PHOTONICS Research

Coherent supercontinuum generation in soft glass photonic crystal fibers

Mariusz Klimczak,[1,*] Bartłomiej Siwicki,[1] Alexander Heidt,[2] and Ryszard Buczyński[1,3]

[1]Glass Department, Institute of Electronic Materials Technology, Wolczynska 133, 01-919 Warsaw, Poland
[2]Institute of Applied Physics, University of Bern, Sidlerstrasse 5, CH-3012 Bern, Switzerland
[3]Faculty of Physics, University of Warsaw, Pasteura 7, 02-093 Warsaw, Poland
*Corresponding author: mariusz.klimczak@itme.edu.pl

Received 31 July 2017; revised 22 October 2017; accepted 23 October 2017; posted 24 October 2017 (Doc. ID 303581); published 17 November 2017

An overview of the progress on pulse-preserving, coherent, nonlinear fiber-based supercontinuum generation is presented. The context encompasses various wavelength ranges and pump sources, starting with silica photonic crystal fibers pumped with 1.0 μm femtosecond lasers up to chalcogenide step-index and microstructured fibers pumped from optical parametric amplifiers tuned to mid-infrared wavelengths. In particular, silica and silicate-based all-normal dispersion (ANDi) photonic crystal fibers have been demonstrated for pumping with femtosecond lasers operating at 1.56 μm with the recorded spectra covering 0.9–2.3 μm. This matches amplification bands of robust fiber amplifiers and femtosecond lasers. The review therefore focuses specifically on this wavelength range, discussing glass and nonlinear fiber designs, experimental results on supercontinuum generation up to the fundamental limit of oxide glass fiber transmission around 2.8 μm, and various limitations of supercontinuum bandwidth and coherence. Specifically, the role of nonlinear response against the role of dispersion profile shape is analyzed for two different soft glass ANDi fibers pumped at more than 2.0 μm. A spatio-temporal interaction of the fundamental fiber mode with modes propagating in the photonic lattice of the discussed ANDi fibers is shown to have positive effects on the coherence of the supercontinuum at pump pulse durations of 400 fs. Finally, the design and development of graded-index, nanostructured core optical fibers are discussed. In such structures the arbitrary shaping of the core refractive index profile could significantly improve the engineering flexibility of dispersion and effective mode area characteristics, and would be an interesting platform to further study the intermodal interaction mechanisms and their impact on supercontinuum coherence for sub-picosecond laser pumped setups.

OCIS codes: (190.4370) Nonlinear optics, fibers; (060.5295) Photonic crystal fibers; (320.6629) Supercontinuum generation.

https://doi.org/10.1364/PRJ.5.000710

1. INTRODUCTION

The development of light sources delivering ultra-short pulses of ultra-high quality is stimulated by imaging applications [1], by the generation of ultra-stable optical frequency combs [2], and by other areas concentrated on processes occurring over very short timescales or with very low repeatability [3]. Such sources should be characterized with high brightness, broad spectral coverage of generated radiation, and—what is of paramount importance—high phase coherence and spectral coherence. Imaging of biological tissue in optical coherence tomography (OCT) benefits from the change of probing wavelength from 1.3 to 1.7 μm, where the scanning beam experiences less scattering and avoids water absorption peaks [4]. Moreover, application of a shot-to-shot repeatable supercontinuum (SC) light source, delivering spectrum contained entirely within the normal dispersion range of wavelengths of the nonlinear fiber, allows increasing the imaging penetration depth and improving the signal-to-noise rate (SNR) by 10 dB [5]. Similar advantages are obtained with a broadband source operating at a wavelength of around 2 μm and longer for OCT imaging of non-biological matter [6]. A coherently broadened 3.1 ps pulse was used as a seed for an optical frequency comb, in one of the first reports, enabling C-band coverage with 365 lines (3.64 THz bandwidth) within 6 dB dynamical range. Results were also published demonstrating nearly a factor of 20 increment of the number of channels and in a twice narrower bandwidth, also in the third telecommunication window [7]. The benefits of stability of a broadband, pulsed source were also demonstrated in the context of phase shift keying (PSK) communications [8]. Bit error rate (BER) was compared here in a transmission experiment,

where a frequency comb source used as the reference was pumped with either anomalous dispersion-pumped SC or an all-normal dispersion (ANDi) SC. The use of the latter source resulted in negligible influence of BER on PSK transmission.

In this work, we provide an overview of the most recent results and state-of-the-art in coherent pulse-preserving SC generation in nonlinear optical fibers. We begin with the fundamentals on SC generation with emphasis given to noise-seeded and self-seeded operation. While a broad scope of silica, silicate, and non-oxide glass ANDi fibers are recalled in the context of either numerical or experimental SC generation throughout the work, particular attention is given to lead-silicate and boron-silicate soft glass ANDi photonic crystal fibers (PCFs) now routinely fabricated by the Glass Department group at the Institute of Electronic Materials Technology (ITME). The introduction is followed by a detailed description of these glasses and PCF structures used throughout rest of the work. Complete information on critical optical parameters and geometric dimensions of physically fabricated fibers are provided. Next, SC generation in ANDi fibers is addressed directly, beginning with nonlinear modeling and discussion of a typical, femtosecond pulse-pumped sequence of nonlinear processes leading to the formation of high-quality, coherent SC pulses. An overview of experimental results of ANDi SC results is given, indicating glass of the fiber, pump pulse duration, and wavelength, as well as the recorded spectral width.

Coherence and pulse preservation in ANDi SC are related in the sense that self-seeded nonlinear processes are required to dominate formation of the SC pulses. Femtosecond pumping is generally regarded as required to assure that. In order to explore the possibilities to soften this requirement, a new means of coherence preservation is proposed—one exploiting deterministic seeding interaction between the lattice modes of the discussed all-solid ANDi PCFs and their nonlinear, fundamental mode of the core.

The final section of our review highlights the introduction of nanostructures in the fiber core as a new means towards engineering the graded-index fibers. The proposed method, fundamentally rooted in the effective medium theory [9], allows the design and fabrication of fibers with arbitrary core refractive index profiles, not confined to circular or elliptical shapes imposed by the current vapor deposition technologies. In the ANDi SC context, this new approach potentially opens up routes to separate the interdependence of the dispersion profile and the effective mode area and design both independently up to a certain degree. This could have a positive effect on the strength of the nonlinear response in the final fibers while still maintaining full control over the dispersion profile.

2. SC GENERATION FUNDAMENTALS

SC generation was demonstrated for the first time in 1970 by Alfano and Shapiro in a bulk boron-silicate glass [10], and since then it has started to play an increasingly pronounced role in nonlinear optics [11]. The medium of choice for SC generation in the past two decades has been the optical fiber, and in particular the PCF (microstructured fiber), for reasons including good spatial confinement enhancing nonlinearity and facilitating spatial coherence of the pump laser, as well as enabling significant flexibility in the dispersion design of the fiber [11,12].

The phase coherence of an SC source is a distinct problem in the area of nonlinear fiber optics research. Existing state-of-the-art draws a clear relation between SC phase coherence and the duration of the pump pulse [13]. The sign of the chromatic dispersion profile in the wavelength range covered by the SC also has a share of influence over this property [11].

Optical pumping with pulses lasting 100 fs or less, centered at a wavelength of anomalous dispersion of the nonlinear medium, typically favors processes of self-phase modulation (SPM) and soliton fission (SF), as well as the solitons' gradual (along the propagation direction) decrease of frequency due to Raman scattering [soliton self-frequency shift (SSFS)]. The resulting spectrum maintains high phase coherence in a bandwidth of hundreds of terahertzs [13]. In general, every continuous-wave signal with sufficiently high intensity of the electric field experiences break-up into a train of pulses due to modulation instability (MI) [14]. The combined effects of soliton dynamics and MI are crucial to the high efficiency in terms of the spectral width of such sources, despite their phase incoherence [11,13]. In fibers made from unconventional glasses, such an approach enabled SC generation stretching from around 1 μm up to the mid-infrared around 5 μm (tellurite glass fibers [15] or fluorozirconate, ZBLAN-type glass fibers [16]) or even up to 13 μm in multimode fibers made from chalcogenide glasses [17]. Broadband solitonic supercontinua across the near-infrared have also been demonstrated in PCFs designed and fabricated at ITME with lead–bismuth–gallate oxide [18,19] or tellurium oxide glasses [20].

Pulse duration is not the sole indicator distinguishing between a coherent or incoherent spectral broadening process in a nonlinear optical material. In case of some anomalous dispersion-pumped, octave-spanning spectra, a considerable drop of coherence has been anticipated numerically for pump pulses as short as 50 fs [13]. For the estimation of coherence properties, the characteristic length scales of SF and MI in a fiber have to be considered, which are defined as follows [21]:

$$L_{\text{fiss}} = L_{\text{D}}/L_{\text{NL}}, \quad L_{\text{MI}} \sim 16L_{\text{NL}}, \quad L_{\text{D}} = t_0^2/|\beta_2|,$$
$$N = L_{\text{D}}/L_{\text{NL}} \quad \text{and} \quad L_{\text{NL}} = 1/(\gamma P_0), \tag{1}$$

where L_{fiss} is the SF characteristic length scale, L_{MI} is the MI characteristic length scale, L_{D} is the dispersive characteristic length scale, L_{NL} is the nonlinear characteristic length scale, t_0 is the time duration of the pump pulse, β_2 is the group velocity dispersion at the pump center wavelength, γ is the nonlinear coefficient, and P_0 is the pump pulse peak power. Depending on the relation of L_{fiss} and L_{MI}, either coherent SF-driven or incoherent noise-driven SC are generated [11].

In the wavelength range with normal dispersion, where solitons are not supported, MI and related decoherence can also take place [22]. In such a case, Raman scattering is dominant, while four-wave mixing (FWM) and MI is only phase-matched due to the presence of the former. The two effects

merge into one effective noise-amplifying nonlinear process [23]. Fiber birefringence has also been identified as a possible source of normal dispersion SC instability [24,25].

Phase coherence and spectral stability of SC can be facilitated with different means. Pumping with very short pulses (≤50 fs)—taking into account the length of the nonlinear medium in relation to the characteristic length scales [Eq. (1)] and the input soliton order—is the most straightforward solution. A low-power seed signal can also be in-coupled to the fiber (often a continuous-wave signal) at a wavelength corresponding to SC fragments affected by MI amplification of noise. The purpose of the seed signal is delivering spectral components with pulse-to-pulse deterministic phase [26–28]. An alternative way is the use of a tapered fiber as the nonlinear medium [29]. In such a fiber, the broadening begins in the part of fiber with anomalous chromatic dispersion at the pump wavelength. The dispersion profile then evolves along the structure towards normal dispersion, before soliton-pumped amplification of noise can take place under the pump conditions intended for such a structure at the design stage. Results of numerical simulations suggest that pulse-to-pulse SC decoherence can be substantially reduced in just a slightly tapered fiber pumped with self-similarity pre-compressed pulses [30]. This would in turn enable pumping with a relatively simple picosecond laser system. However, so far this concept cannot be demonstrated experimentally. Yet another alternative is containing of the SC spectrum entirely within the wavelength range, where there is normal dispersion in the nonlinear medium (ANDi). Together with femtosecond pumping, a coherent SC with a flat spectrum spanning over octave bandwidths has been demonstrated in the near-infrared [31–36] in silica or lead-silicate glass fibers or in chalcogenide glass fibers in the mid-infrared up to 5–6 μm [37–39]. Compared to solitonic and especially MI-driven supercontinua, its ANDi counterparts are generally considered less efficient in terms of obtainable spectrum for similar pump pulse energy and duration. This can be explained with the following: while MI-driven, soliton SC relies simply on spectrally abundant background noise as the seed signal, the femtosecond ANDi SC is intrinsically self-seeded. Under femtosecond pumping, a coherent SC can be readily obtained when the pump wavelength falls into anomalous dispersion, and, apart from SPM, the soliton/dispersive wave dynamics contribute to spectral broadening and the spectrum usually has broader bandwidth compared to ANDi generation [40,41]. The true advantage of femtosecond-pumped ANDi SC therefore stems from its pulse-preserving feature, related to the fact that the dispersion profile of fiber does not change the sign (remains normal) across the SC wavelengths. Pulse preservation and low contribution of higher order dispersion terms into the ANDi broadening opens the route to robust, fiber-based sources of ultra-short pulses, at the order of below two optical cycles duration, with applications in highly time-resolved measurements of bio-chemical or physical processes in matter [42–44]. It is notable that ANDi SC produces very flat and uniform spectra, compared to conventional, anomalous dispersion-pumped SC. The coherence property will also be maintained under pumping with pulses much longer than tens or low hundreds of femtoseconds, although the spectral width will be much below an octave.

3. GLASS AND FIBER DESIGN

The main limitation of the "classic" air-hole lattice/microstructured PCFs in the context of dispersion engineering boils down to the limits set out by the material dispersion of used glass. With the air refractive index reasonably assumed as wavelength-independent, it is the fixed material dispersion that has to be compensated with the waveguide contribution tailored by the PCF microstructure layout. Gases or liquids can be introduced into the lattice to extend the design flexibility [45,46], but at a significant cost of robustness and handling convenience.

All this can be worked around if the air holes of the "classic" PCF lattice are substituted by inclusions made of a different, thermally matched glass. In such all-solid glass PCFs made of two thermally matched glasses, there is also a possibility to influence the chromatic dispersion profile by manipulating the material dispersion contribution. A PCF with an all-solid glass structure was demonstrated for the first time by Feng *et al.* [47]. Construction of an all-solid structured fiber requires at least two glasses with different refractive indices, but with thermal properties matched as close as possible. It is especially important to assure similar values of the thermal expansion coefficients and the characteristic temperatures. Such structures, designed specifically with coherent SC generation in mind, were first demonstrated by Buczyński and co-workers [48]. They had their core and lattice made of the commercially available F2 glass (Schott). The lattice inclusions were made of boron-silicate glass developed in-house and melted in the Glass Department laboratory at ITME. The composition of this glass labeled NC21A is as follows: (mol.%) SiO_2, 56.84; B_2O_3, 23.19; Al_2O_3, 0.61; Li_2O, 6.23; Na_2O, 9.51; K_2O, 3.63. The refractive indices measured at a wavelength of 1550 nm for the two glasses are $n_{F2} = 1.59487$ and $n_{NC21A} = 1.51130$, respectively. Therefore the fiber guides light by total internal reflection. The glass transition temperatures for the two glasses are $Tg_{F2} = 569°C$ and $Tg_{NC21A} = 492°C$. Nonlinear refractive indices, measured at 1240 nm [49], are $n_2 = 2.9 \times 10^{-20}$ m^2/W (F2) and $n_2 = 1.1 \times 10^{-20}$ m^2/W (NC21A).

A variant of this PCF lattice type was demonstrated recently [35] with the use of solely commercial glasses F2 (lattice inclusions and surrounding tube) and SF6 (core and hexagonal lattice), both from Schott. A typical image of the PCF microstructure is shown in a scanning electron microscopy (SEM) image in Fig. 1. An obvious advantage of the new design is the use of highly nonlinear SF6 glass for the core with $n_2 = 21 \times 10^{-20}$ m^2/W—measured at 1500 nm [50]. The transition temperature of SF6 is $Tg_{SF6} = 423°C$; therefore it is thermally matched to F2. The linear refractive index of SF6 measured at a wavelength of 1550 nm is $n_{SF6} = 1.764133$, allowing for index-guiding fiber designs with F2 glass. None of the three glasses (NC21A, F2, SF6) is thermally matched to a lead–bismuth–gallate oxide glass (PBG08), which was used for the development of nonlinear PCFs for noise-driven SC across the near-infrared [18,19]. The composition of this glass is as follows: (% mass) PbO, 39.17; Bi_2O_3, 27.26; Ga_2O_3, 14.26; CdO, 5.26; SiO_2, 14.6; $T_g = 484°C$. Interestingly, its transmission window extends from below

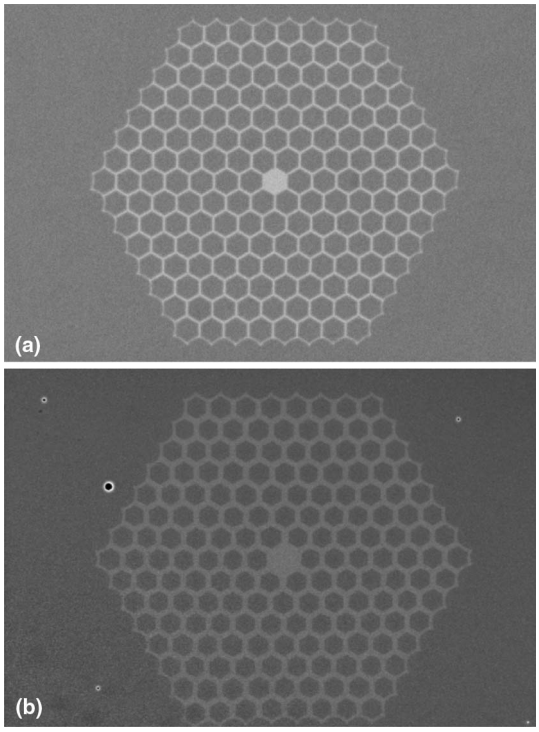

Fig. 1. SEM images of all-solid soft glass ANDi PCFs. (a) NL21 series: core and hexagonal lattice (light color) made of F2 glass, lattice inclusions and lattice surrounding made of NC21A glass. (b) NL38 series: SF6 in the core and lattice, F2 in the inclusions and the surrounding tube.

0.5 μm to around 5.0 μm; however, a strong and difficult to eliminate OH^- absorption band at 2.8–3.1 μm has hindered the utilization of this potential in optical fibers. This glass can be thermally matched to a UV-extended silicate-based glass with the following composition: (% mass) SiO_2, 53; K_2O, 7.5; Na_2O, 5; Li_2O, 5; B_2O_3, 28; Al_2O_3, 1.5; $Tg = 495°C$, labeled UV710. This rather unusual combination would allow us to exploit the PBG08 high nonlinear refractive index $n_2 = 43 \times 10^{-20}$ m^2/W, exceeding that of SF6 glass. The linear refractive indices of the glasses, measured at a wavelength of 1550 nm, are $n_{PBG08} = 1.88772$ and $n_{UV710} = 1.51065$. Although not demonstrated yet physically, linear simulations for selected topologies designed with this pair of glasses suggest similar linear properties to fiber designed with the pairs NC21A/F2 and F2/SF6. Together with the high nonlinear refractive index of PBG08, this glass combination is very promising for applications in ANDi PCF development.

All three designs of fibers share a hexagonal lattice design, as shown in Fig. 1. Geometrical parameters of the lattice of selected fabricated fibers are summarized in Table 1 and include the NL21 series (NC21A/F2 glasses) and the NL38 series PCFs (F2/SF6 glasses). Table 1 also includes lattice parameters of PCFs potentially possible to draw using UV710 and PBG08 glasses—these are labeled with digits representing three individual simulations. The dispersion profiles calculated for these parameter sets are shown in Fig. 2.

In the case of all glass pair combinations, the larger the lattice parameters, specifically the core diameter and the lattice inclusion relative size (see Table 1), the flatter the "saddle section" of the dispersion profile. For the NL21C2 fiber, it is within ±10 ps/nm/km over 900–2600 nm wavelengths (2600–2700 nm is the practical limit of the fiber's transmission window). While this would be beneficial for the optical wave breaking (OWB) process constituting the spectral broadening of ANDi SC (due to low FWM component offset), it is to be noted that this fiber's effective mode area at 2200 nm is already more than 10 μm^2. Dispersion of the PCF nonlinearity, reasonably assuming wavelength-independent nonlinear refractive index, can be controlled by manipulation of the wavelength-dependent effective mode area. The nonlinear coefficient of an optical fiber is expressed as $\gamma = n_2 \cdot \omega_0/(c \cdot A_{eff})$; therefore it scales approximately as $\gamma \sim A_{eff}^{-1}$; i.e., the nonlinear coefficient drops linearly with the increase of the effective mode area [21]. Hence, there is a tradeoff between chromatic dispersion flatness and effective nonlinearity for all fibers summarized in Table 1, as increasing the core diameter flattens out the dispersion, but also increases A_{eff} and consequently reduces γ. Comparing the wavelength dependence of effective mode areas in the fibers, it can be noticed that the NL21 series shows the strongest variation of all types. In this fiber, A_{eff} grows rapidly already at 2500 nm, while the potential UV710-PBG08 design labeled "3" should have relatively flat A_{eff} profile up to about 3000 nm, which is already beyond the fiber's transmission window.

Table 1. Overview of Lattice Parameters of All-Solid Soft Glass PCFs with Engineered Normal Dispersion Profiles

NL21 Series	Outer Diameter [μm]	Core Size [μm]	Inclusion Size d [μm]	Relative Inclusion Size d/Λ
C2	155.0	2.46	2.3	0.90
C3	148.4	2.46	2.2	0.90
C4	142.8	2.46	2.16	0.89
NL38 Series	**Outer Diameter [μm]**	**Core Size [μm]**	**Inclusion Size d [μm]**	**Relative Inclusion Size d/Λ**
C1	126.0	2.36	1.30	0.79
C2	132.5	2.53	1.39	0.77
C3	132.6	2.49	1.33	0.77
C4	135.4	2.44	1.38	0.77
UV710 + PBG08 Concept PCF	**Outer Diameter [μm]**	**Core Size [μm]**	**Inclusion Size d [μm]**	**Relative Inclusion Size d/Λ**
1	125.0	3.84	0.94	0.40
2	125.0	3.00	1.00	0.50
3	125.0	2.49	1.33	0.77

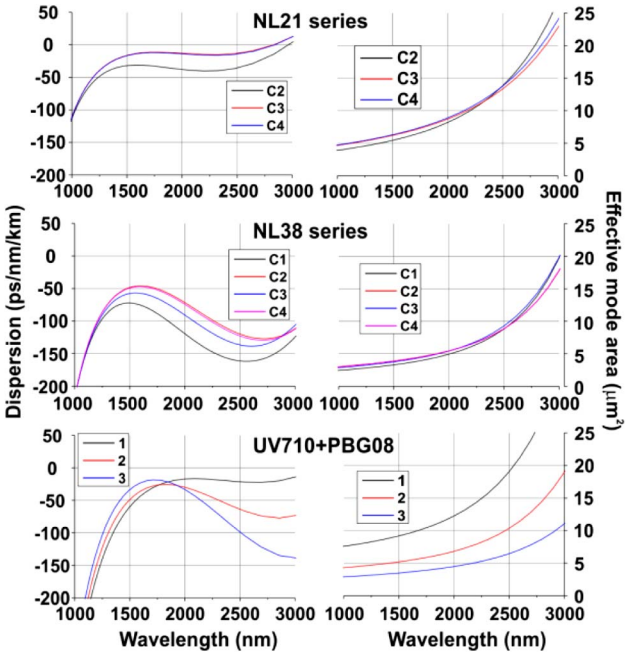

Fig. 2. Dispersion profiles and effective mode areas obtained in numerical simulations for the all-solid glass ANDi PCFs: (a), (b) NL21 series; (c), (d) NL38 series; (e), (f) UV710 + PBG08 fibers.

The tradeoff between chromatic dispersion flatness and effective nonlinearity and their influence on the obtainable SC bandwidth has been recently discussed using simulations and measurements SC in the NL21 and NL38 series fibers [35].

4. ANDI SC MODELING

A rigorously parametrized generalized nonlinear Schroedinger equation (GNLSE) model enables us to predict the performance of ANDi nonlinear fiber with impressive precision. The sequence of nonlinear processes composing the spectral formation in femtosecond-pumped ANDi SC has been discussed in detail [51,52]. The entire process can occur fast over typical nonlinear fiber lengths, as shown in Fig. 3(a). At the initial stage, the spectrum broadens due to SPM—it is manifested by the characteristic "*S*" shape of the time-wavelength profile; see the numerical spectrogram in Fig. 3(b). The next phase begins with modulation at the leading and trailing edges of the propagating SC pulse (in the time domain), which is generally assigned to the effect of OWB. In the spectral domain, this corresponds to the beating between the new

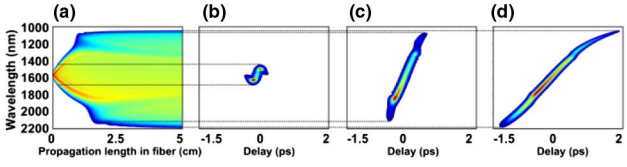

Fig. 3. Sequence of physical processes broadening the ultra-short laser pulse in an ANDi fiber. (a) Evolution of the spectrum along the entire nonlinear fiber length. (b)–(d) Numerical spectrograms.

OWB features and the parts of spectrum where OWB is yet to occur (or the other way, depending on the direction of wavelength shifting) [Fig. 3(c)]. From the time domain perspective, mixing takes place between the SPM components and pulse front or pulse tail, which contains the original center frequency of the pulse. The results are the OWB sidebands completing the spectrum [Fig. 3(d)].

Notably, the ANDi nonlinear process described above occurs fast—that is, over the initial centimeters of the fiber length. This is achieved by such a selection of the geometrical parameters of the photonic lattice that there is a proper balance between the linear effects (dispersion) and the nonlinear effects (SPM and OWB initiated FWM). The short propagation length, over which the spectrum is formed, has tremendous meaning to PCFs drawn from soft glasses, as these fibers usually suffer from larger attenuation compared to silica fibers. Fluoride fibers would be an exception in that their loss is usually very low. However, dispersion engineering in fluoride glass fibers is challenging due to the difficult glass technology, and very few ANDi SC results in fluoride glasses have been reported [38]. Attenuation of the NL21 series fibers is at the level of 2–3 dB/m. The discussed process occurring under pumping such as the one used in the works [53,54] is coherent in the sense that it is phase-preserving from shot to shot. This is because the SPM and OWB processes are intrinsically self-seeded. The roughly 70 fs pump pulse duration is short enough so that the Raman response of the fiber glass, which is delayed against the Kerr nonlinearity response, does not significantly influence the spectral broadening in the perspective of the pump pulse duration. The all-solid glass PCF designs, summarized in the preceding section, offer a new solution allowing them to influence and potentially to control the coherence properties in SC generation.

5. ANDI SC GENERATION IN PHYSICAL FIBERS

A. Review of State of the Art

This work treats SC generation mainly from the soft glass perspective, and it is important to begin reviewing the state-of-the-art by stressing the motivation for selecting this material platform. Despite inferior mechanical properties compared to silica, soft glass fibers have the advantage of much broader transmission windows, covering the mid-infrared wavelengths. Moreover, in nonlinear optics applications, the high values of the nonlinear refractive index of most soft glasses usually more than compensate for their higher background loss compared to silica fibers. Indeed, extensive research has resulted in reports on SC generation covering the near- and mid-infrared wavelengths from about 1 μm up to even 15 μm in either step–step index or suspended core chalcogenide glass fibers [16,17,55,56]. Owning to the high nonlinearity and the combination of visible and mid-infrared transmission in certain chalcogenide glasses, hybrid chalcogenide–tellurite glass fibers have been demonstrated for tunable third-harmonic generation [57]. Tellurite oxide glass fibers, having narrower transmission windows than chalcogenides, but benefitting from better mechanical properties, have also been investigated for mid-infrared SC generation up to about 5 μm [15,58–61], as well in fiber parametric amplifiers [62]. It is worth noting that

Table 2. Coherent, Pulse-Preserving SC Generation in ANDi Fibers[a]

#	Fiber Glass	Pump Wavelength [nm]	Pump Pulse Duration	SC Spectral Width [nm]	Reported Dyn. Range [dB]	Ref.	Year of Publication
1.	$AsSe_2/As_2S_5$	2700	200 fs	2200–3300	35	[39]	2016
2.	Ge:SiO_2	1560	23 fs	1100–2200	30	[36]	2016
3.	As_2S_3	3830	300 fs	3000–4800	20	[37]	2015
4.	SiO_2, PM fiber	1041	229 fs	750–1300	–	[25]	2015
5.	F2/NC21A all-solid glass PCF	2160	60 fs	950–2550	10	[35]	2015
6.	SF6/F2 all-solid glass PCF	2160	60 fs	1100–2700	20	[35]	2015
7.	F2/NC21A all-solid glass PCF	1550	75 fs	950–2300	<10	[54]	2014
8.	SiO_2	1064	350 fs	700–1400	10	[31]	2011
9.	SiO_2	650/790/1050	50 fs	600–1500 425–900	20	[32]	2011
10.	SiO_2	625	50 fs	370–895	20	[68]	2011
11.	SiO_2	1690	110 fs	1100–2100	20	[33]	2007
12.	SiO_2	1552	712 fs	1400–1725	20	[69]	1998
13.	BK-7 (bulk glass)	530	4–8 ps	400–700	–	[10]	1970

[a]Experimental Results; PM, polarization maintaining.

tellurite glasses are a particularly versatile group of materials for fibers. Tellurite optical fibers have been reported having two embedded metal electrodes, thus combining optical and electrical functionalities [63]. Various fluoride non-oxide glasses, including ZBLAN, are currently and unquestionably the most important materials for mid-infrared SC generation in fibers [16,64,65]. Recently, a PCF made of ZBLAN glass was reported with enhanced performance of SC generation in the ultraviolet wavelength range [66]. Despite the fact that their nonlinearity is comparable to silica and their transmission window in optical fibers limits practical SC generation to usually 4–5 μm, ZBLAN fibers enabled the introduction of mid-infrared SC sources as commercially available devices by several vendors [67].

Coherent and pulse-preserving SC generation is particularly dependent on the strength of the nonlinear response of the entire system. From the fundamental perspective of the physics of the process, it requires pumping with femtosecond laser pulses. Nevertheless, the high nonlinearity intrinsic to most soft glass fibers has also been shown to be very supportive in extending such SC spectra towards the red [35].

Table 2 lists a selection of the most important results in recent literature on coherent SC generation in ANDi fibers. Most results to date have been obtained in PCFs, the result reported by Kadenburg *et al.* on mid-infrared ANDi SC being an exception in this lineup [37,39,52]. Femtosecond pump sources in these experiments were typically complex, tunable optical parametric amplifiers (OPAs), which deliver pulses lasting around 50–100 fs with ample energy. In the case of chalcogenide fibers, the wavelength tunability of OPAs was necessitated by the lack of alternatives in mid-infrared femtosecond laser systems. In the cases of near-infrared pumping of silica and silicate glass ANDi fibers, the strengths were often convenience and availability for particular experiments, while femtosecond lasers at fixed wavelengths compatible with these fibers were available as well. While Table 2 shows experimental data, a significant number of theoretical (numerical) simulations on ANDi SC generation have been published as well, and a reading list could include SC generation in silica PCFs [51,70], Ge-doped silica PCFs [71,72], and chalcogenide glass PCFs or waveguides [39].

Pulse-preserving ANDi SC spectra spanning at least an octave are readily obtained under pumping with a range of sub-picosecond laser sources. Pure silica glass enables dispersion engineering for the Ti:sapphire and ytterbium laser wavelengths (790 nm and around 1050 nm), although PCF designs compatible with erbium pump lasers have also been demonstrated (1560 nm and Raman-shifted 1560 to 1690 nm). Oxide soft glass PCFs, including the designs recalled in detail in this work, are compatible with erbium laser wavelengths, as well as with the emerging thulium lasers (1900–2100 nm). These fibers enable us to cover wavelengths from the visible to around 2800 nm, which is the limit of transmission of silica and silicate-type glasses. Mid-infrared pulse-preserving supercontinua can be realized in chalcogenide fibers as shown in recent years—see Table 2. However, chalcogenide glass has a very steep normal dispersion slope at wavelengths of typical, efficient mode-locked fiber lasers, specifically ytterbium, erbium, and thulium (1.0, 1.5, and 2.0 μm), and octave-spanning, femtosecond SC generation in these PCFs—although possible—requires exotic mid-infrared pump wavelengths available only from OPA systems. In the lineup shown in Table 2, the all-solid oxide soft glass PCFs demonstrate a convenient compromise of at least three practical features: the transmission window, the nonlinear response, and the material dispersion enabling design of PCFs compatible with standard laser wavelengths. In other words, although the mid-infrared part of the spectrum is inaccessible with these materials, the fibers made from these glasses enable further reach into the infrared than silica PCFs and still under pumping with typical wavelengths available from fiber-based mode-locked lasers, which are becoming a standard [73,74]. Almost all of the results listed in Table 2 were reported in polarization

non-maintaining fibers, and the polarization context has indeed been omitted in the bulk of ANDi SC research.

Form birefringence of ANDi PCFs has been found to influence the coherence properties of ANDi SC [24,25,75]. Birefringence as small as 10^{-5} stemming from PCF structure imperfections introduced during fiber drawing has been identified to hinder ANDi SC pulse recompression, which was not observed in a polarization maintaining (PM) ANDi PCF SC investigated for reference [75]. Although no significant phase decoherence has been observed in these experiments, it was later reported that spectral instability, not detectable in PM fiber ANDi SC, could be recorded even in weakly birefringent fibers [24]. It has been further determined that form birefringence-related noise in ANDi SC was seeded by random field distributions between the two orthogonal polarizations of the PCF [25].

B. Pulse-Preserving SC in Soft Glass Fibers Pumped at 1560 nm

A comprehensive report on ANDi SC generation in soft glass PCFs was delivered in the work [54]. The structure of the fibers used corresponded to the all-solid hexagonal lattice PCFs discussed in the preceding section. Through the change of geometrical parameters, such as the diameters of the core and the photonic cladding, the pitch, and the relative inclusion size, the team designed a family of fibers with chromatic dispersion shown in Fig. 4. The geometrical parameters of the fibers in that particular series are listed in Table 3.

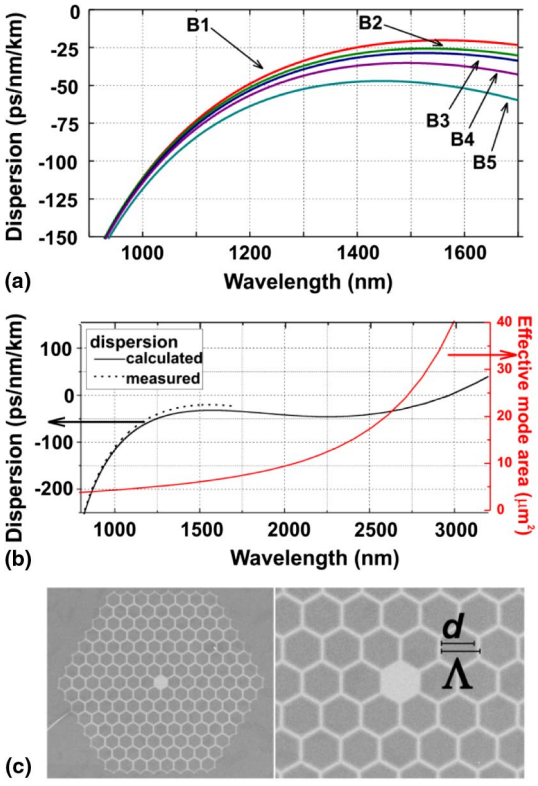

Fig. 4. (a) Measured chromatic dispersion profiles of the fabricated fibers, (b) dispersion profile (measured and theoretical) and the wavelength dependence of the effective mode area of the B1 fiber, and (c) SEM images of this particular fiber.

Table 3. Geometrical Parameters of the Series of All-Solid Glass PCFs with ANDi, as used in Ref. [54]

PCF No.	Outer Diam. [μm]	Lattice Diagonal [μm]	Width of the Core [μm]	Inclusion Diam. [μm]	d/Λ
B1	143.0	35.61	2.43	2.15	0.91
B2	140.3	35.06	2.40	2.13	0.91
B3	136.6	34.65	2.37	2.11	0.91
B4	131.0	33.33	2.25	1.99	0.91
B5	128.8	31.55	2.13	1.93	0.91

The fabricated fibers have almost flat dispersion profiles in a wide range of wavelengths. The change of the lattice geometrical parameters (decrease of overall lattice size) results in the change (increment) of the absolute value of dispersion of the flattened section of the dispersion profile, as well as a red-shifting of its local maximum. Detailed studies of these dependencies were conducted earlier [76]. The family of SC spectra, recorded in the fabricated fibers under pumping with 70 fs pulses centered at 1550 nm, is shown in Fig. 5(a). The pump source in these experiments was an OPA. In the best case (fiber B1) the spectrum spanned a wavelength range from 900 to 2300 nm. These results are comparable and exceed only slightly the SC widths reported in air-hole silica or silica–germanium PCFs pumped with femtosecond pulses around 1.5–1.6 μm [33,36].

The comparison of experimental and numerical results reported for soft glass NL21 series PCFs in [54] is shown in Fig. 5(b). The discrepancy between experiment and simulation around the pump wavelength was assigned to unconverted pump pulse energy guided in the photonic cladding, which does

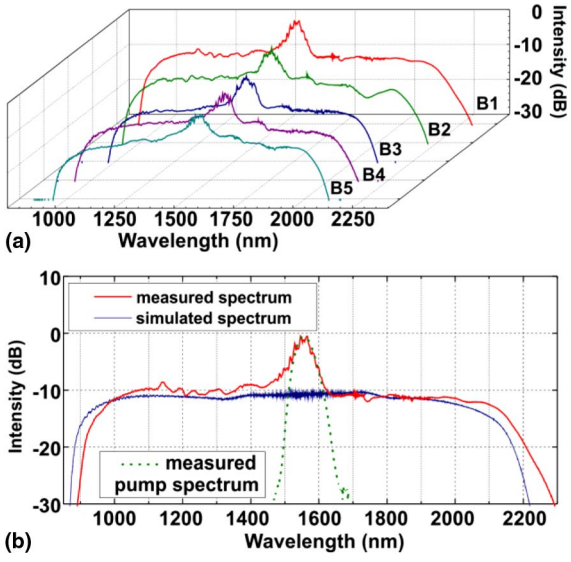

Fig. 5. (a) SC spectra recorded for the ANDi fibers listed in Table 3, measured under pumping with 70 fs centered at 1550 nm, and (b) broadest recorded spectrum in the NL21B1 fiber, its numerical reconstruction with a GNLSE model and measured pump laser spectrum [54].

not participate in the nonlinear broadening process under these pump pulse durations (<100 fs). For longer pump pulses, the interaction between the lattice-confined, unconverted pump radiation and the nonlinearly guided mode in the core has been found to mitigate SC decoherence [77,78]—which will be discussed in the following section.

C. Pulse-Preserving SC in Soft Glass Fibers Pumped at >2000 nm

Ultra-fast femtosecond lasers based on Tm, Tm/Ho, or Ho-doped fibers operating at 1.9–2.0 μm and beyond are becoming available, not only at laboratories [73,74,79,80] but also at major vendors [41]. Available literature often points out applications of such laser systems in SC generation, especially that pump wavelengths around 2 μm are compatible with fluoride glass fibers and enable solitonic SC generation across near-infrared and mid-infrared wavelengths. With the flattened "saddle" section of the soft glass PCFs discussed here, extending from below 1.0 μm up to the transmission cutoff of silicate glasses at about 2.8 μm, these fibers are natural candidates for these new 2.0 μm femtosecond lasers and extension of pulse-preserving SC generation towards the mid-infrared. In order to explore these possibilities, SC generation in NL21 and NL38 series fibers has been investigated under pumping with femtosecond pulses at wavelengths exceeding 2 μm [35]. Specifically, an OPA system delivering 60 fs pulses tuned to a wavelength of 2160 nm has been used. Two types of fibers from each PCF family have been used in experiments; their geometric and optical parameters are summarized in Tables 4 and 5. SC spectra obtained in 30-cm-long samples are shown in Fig. 6. Optical power values refer to average powers incident on the fiber input facet in each case. The NL38 fibers proved much more resistant to optical power damage and could be pumped stronger than the NL21 series,

Table 4. Geometrical Parameters of NL21 and NL38 Series Fibers used in Experiments with Femtosecond Pumping at a Wavelength >2.0 μm

Fiber designation	NL21C2	NL21C4	NL38A2	NL38A4
Inclusion size [μm]	2.3	2.2	1.25	1.2
Lattice constant [μm]	2.56	2.41	1.55	1.54
Core diameter [μm]	2.46	2.46	2.27	2.21
Lattice diameter [μm]	38.0	35.6	25.3	24.6
Outer diameter [μm]	155	143	120	117

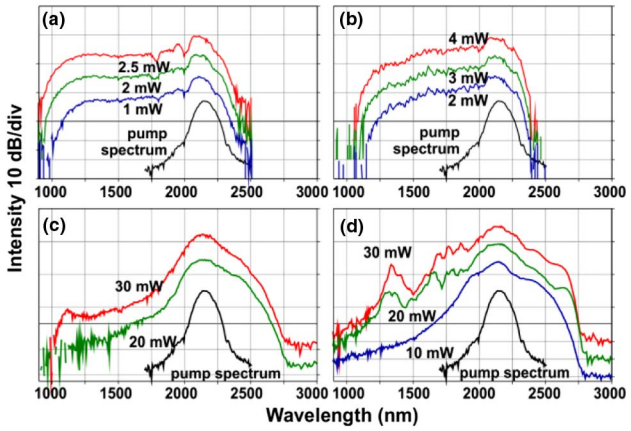

Fig. 6. SC spectra measured in the all-solid soft glass ANDi PCFs under 2160 nm femtosecond pumping. (a) NL21C2, (b) NL21C4, (c) NL38A2, and (d) NL38A4 [35].

although similar results to those shown in Figs. 6(c) and 6(d) were obtainable at incident average power levels comparable to those indicated for the NL21 fibers. It is notable that only NL38 fibers exhibit any red-shifted spectral broadening, with the broadest spectrum reaching the transmission cutoff of the fiber at about 2800 nm. In the NL21 fibers, the red-shifted part of spectrum turned out to be practically limited to the extent of the pump spectrum.

The explanation of these differences in spectral broadening efficiency is related to the tradeoff of dispersion flatness and nonlinearity already discussed in the previous section. The fiber attenuation was ruled out as a decisive factor on its own [35]. Figure 7(a) shows calculated effective mode areas and Fig. 7(b) the dispersion profiles of the two types of fibers. Due to higher index contrast between the glasses of NL38 PCFs than between constituent glasses in the NL21 lattice, the NL38 fibers have roughly half the effective area at 2400 nm than the NL21 fibers. On the other hand, NL21 fibers enabled us to engineer flatter dispersion profiles due to similar curvatures of the material dispersion profiles of the constituent glasses [81].

Nonlinear simulations based on a GNLSE similar to the one described in preceding sections were performed for the following scenarios: wavelength-dependent effective mode area and fiber loss included in the model, model including fiber loss but with A_{eff} fixed to the value at the pump wavelength,

Table 5. Nonlinear Optical Parameters of the NL21 and NL38 Type ANDi Fibers at Wavelengths Compatible with Erbium- and Thulium-Doped Laser Systems

	1550 nm		2160 nm	
Fiber	A_{eff} [μm^2]	γ [W^{-1} km^{-1}]	A_{eff} [μm^2]	γ [W^{-1} km^{-1}]
NL21C2	6.2	13.6	11.5	7.6
		$n_2{}^a = 2.9 \times 10^{-20}$ m^2/W		
NL38A2	4.0	213.7	6.5	133.1
		$n_2{}^b = 21 \times 10^{-20}$ m^2/W		

[a]F2 glass, taken after Ref. [49], measured at 1240 nm.
[b]SF6 glass, taken after Ref. [50], reported for 1500 nm.

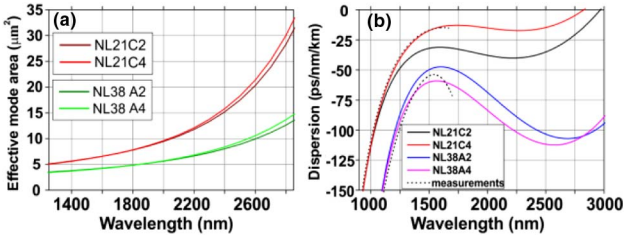

Fig. 7. (a) Calculated effective mode area of the PCFs. (b) Theoretical (solid traces) and measured (dotted traces) dispersion profiles of the PCFs [35].

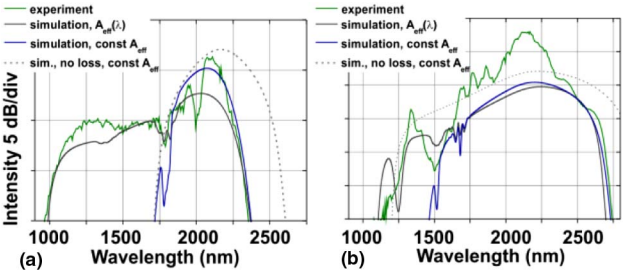

Fig. 8. Reconstruction of experimental results with numerical simulations: (a) NL21C2 fiber, (b) NL38A2 [35].

and a model with a fixed A_{eff} in a lossless PCF. Results for both PCF types are shown in Fig. 8, and the nonlinear optical parameters of the two fibers are given in Table 5.

More than an order of magnitude difference in the nonlinearity of the NL21 and NL38 series of fibers leads to a situation in which the spectral broadening in the NL21 series is mitigated by fiber attenuation at the long-wavelength edge of the pump laser spectrum. In the NL38 fibers, on the other hand, the nonlinearity is strong enough for the broadening to continue up to the fundamental limit of the fiber's transmission window.

6. NEW METHODS OF ENHANCEMENT OF THE COHERENCE PROPERTIES OF SC GENERATION

ANDi coherence properties deteriorate with increasing pump pulse duration, due to an increasing contribution of Raman scattering [23,82]. The rate of this deterioration will depend on the contribution of delayed Raman response to the Kerr nonlinearity. Furthermore, Raman scattering is usually accompanied by FWM [82–84], and even with solitons not supported, the energy is rapidly transferred to the anti-Stokes and Stokes Raman bands of the pump wavelength, and these new components act as pumps in a noise-seeded FWM. Thus noise is amplified even when the nonlinear medium has normal dispersion across all wavelengths of interest.

The phase coherence—that is, phase fluctuation occurring in SC generation from shot to shot—can be evaluated with a standard Michelson type interferometer with unequal path lengths. Results of typical interference measurements for anomalous dispersion-pumped PCFs (NL24 series) and ANDi fibers (NL21 series) are shown in Fig. 9 for different pump powers. The modulus of the complex degree of coherence, carrying the information on the pulse-to-pulse phase variability across a wavelength range, is mathematically defined in the following form:

$$|g_{12}^{(1)}(\lambda, t_1 - t_2 = 0)| = \left| \frac{\langle E_1^*(\lambda, t_1) E_2(\lambda, t_2) \rangle}{[\langle |E_1(\lambda, t_1)|^2 \rangle \langle |E_2(\lambda, t_2)|^2 \rangle]^{1/2}} \right|. \quad (2)$$

The coherence degree was simply inferred from the interference fringe contrast. The pump conditions in all phase-coherence measurements were the same—erbium fiber laser with chirped pulse amplification (CPA), $\lambda_0 = 1560$ nm, $\tau_0 = 400$ fs [85]. The SC pumped into anomalous dispersion (NL24 fiber) reveals phase-coherence properties consistent with expectations. For the smaller input pulse energy [Fig. 9(a)], over a fixed length of fiber the characteristic length scales for nonlinearity and for the MI are favorable for the SPM and SF, rather than for noise amplification. For the larger pump pulse energy

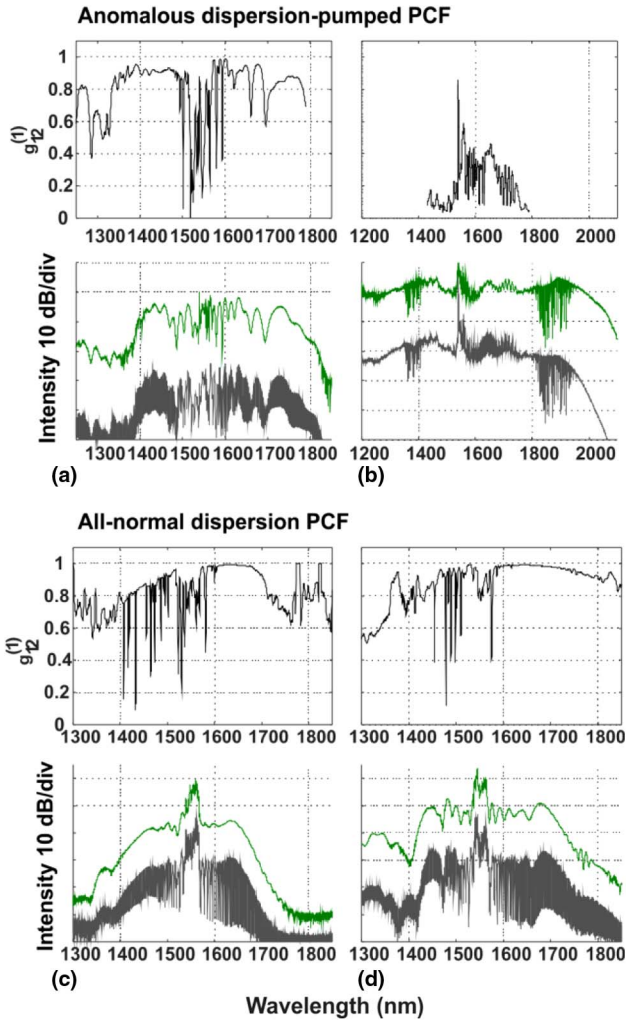

Fig. 9. Results of interference measurements of SC spectra and profiles of spectral degree of coherence: (a) anomalous dispersion-pumped PCF, coupled pump pulse energy $E_{\text{in}} = 2$ nJ; (b) anomalous dispersion-pumped PCF, $E_{\text{in}} = 5$ nJ; (c) ANDi PCF, $E_{\text{in}} = 2$ nJ; and (d) ADNi PCF, $E_{\text{in}} = 5$ nJ [78].

this situation is reversed and noise can be amplified earlier over the fiber sample length; hence the SC experiences decoherence [Fig. 9(b)] [13]. Pumping of SC in the ANDi PCF (NL21) results in coherent SC formation across the complete spectral width and for all investigated input pulse energies, as shown in Figs. 9(c) and 9(d).

Fluctuations of the spectral intensity from shot to shot were resolved with the dispersive Fourier transformation (DFT) method [86–88]. A carefully selected dispersive medium, for example, a single-mode fiber or a pair of diffraction gratings or prisms, can be used to stretch an optical pulse in the time domain. With simultaneous limitation of the pulse energy delivered to the stretcher element, it is possible to avoid its nonlinear response and the pulse spectrum remains unchanged. The chromatic dispersion of the stretcher element should not change sign within the wavelength range covered by the spectrum being resolved. If these conditions are met, then the temporal envelope of the stretched pulse maps into its spectrum. The main components of the used setup were the dispersive medium—1000 or 3700 m (depending on SC spectral width) of DCF-38 fiber with normal dispersion up to about 1900 nm—a fast photodiode with 20 GHz bandwidth, and a fast oscilloscope with 13 GHz bandwidth. The result of the measurement is an oscillogram picturing temporal envelopes of the consecutive pulses.

With maintained linear conditions of stretching in the dispersive element (no nonlinear perturbation of the spectrum of pulses), the frequency scale (and thus the wavelength scale) is obtained from the oscilloscope time-base according to the formula [87,88]

$$T(\omega) = \sum_{m=1}^{\infty} \frac{\beta_{m+1} \cdot z}{m!} \cdot (\omega - \omega_0)^m. \tag{3}$$

Using this scheme, the authors realized time-resolved measurements of the output pulse spectra of the 400 fs pump laser and of the SC pulses with durations of several picoseconds.

DFT measurements allow for linear stretching of pulses originally much shorter than the rise and fall times of available detectors (for the photodiode used in the experiments it was about 140 ps), in the discussed case up to about 10 ns. The length of the dispersion medium that stretches the investigated pulse has to be selected such that the total introduced group delay allows maintaining a satisfactory resolution of the spectrum retrieved from the oscillogram. The upper limit on the stretching is imposed by the overlapping of consecutive pulses. Here, the upper limit was set by the pump laser repetition rate of 40 MHz, corresponding to 25 ns of pulse-to-pulse separation. It is to be noted that a DFT measurement loses phase information and only the single-shot measurement of the pulse spectrum is possible. Measurements of pulse-to-pulse interference are thus required to assess the SC phase coherence.

Spectral intensity stability measurements in both types of fibers, performed with the DFT method, were in agreement with results of coherence measurements in a Michelson interferometer, in a way that there had been a correspondence between a coherent SC pulse and a shot-to-shot stable spectrum [77,78]. In the DFT measurements, ensembles of more than 1200 spectra of consecutive SC pulses were recorded for the NL24 and NL21 fibers. Figure 10 shows the dramatic difference in the shot-to-shot stability of the SC pulses. For the anomalous dispersion-pumped NL24 fiber, the spectral fluctuations exceed 7 dB for most of the covered spectral range. The ANDi spectrum in NL21 fiber also fluctuates, but the amplitude of these variations is significantly smaller, and in almost the entire investigated spectral range it remains below 1 dB, which can be related to factors such as limited dynamic range of the measurement setup (about 20 dB in this case). It is interesting to note the shape of the SNR profiles for both fibers (Fig. 10), which here are the measures of the shot-to-shot spectral fluctuation. First, the SNR for both fibers is similar around the pump wavelength. This is understandable, since higher order modes and cladding modes are excited and the unknown phase profile of the pump has the most influence. In the NL24 fiber the SNR does not improve with the detuning from the pump. In the ANDi fiber the noise is quenched as the spectral sidebands develop. Moreover, the profile of SNR in the NL21 fiber SC has a characteristic train of local maxima extending towards the shorter and longer wavelengths from the pump. For an in-depth analysis of these interesting phenomena, spectral correlation analysis has been used to peek into the relative dynamics among individual spectral components of the generated SC spectra. Spectral correlation analysis of SC has recently been proposed by Dudley and co-workers from the Universite de Franche-Comte in Besançon, France [87,88]. The correlation in this approach is discussed using a map, calculated according to

$$\rho(\lambda_1, \lambda_2) = \left| \frac{\langle I(\lambda_1) I(\lambda_2) \rangle - \langle I(\lambda_1) \rangle \langle I(\lambda_2) \rangle}{\sqrt{(\langle I^2(\lambda_1) \rangle - \langle I(\lambda_1) \rangle^2)(\langle I^2(\lambda_2) \rangle - \langle I(\lambda_2) \rangle^2)}} \right|. \tag{4}$$

The map contains values from −1 to 1. The Cartesian coordinates of the map represent each possible pair of wavelengths in the SC. The value of 1 stands for full correlation—that is, when the intensity at both correlated wavelengths either increases or decreases at a given time. The value of −1 represents a situation in which the two wavelengths are anti-correlated. When the intensity at one of them increases, then that at the other one decreases. The diagonal from the lower-left corner to the upper-right corner contains values of 1, which is a trivial confirmation of every wavelength being at full correlation with itself. The map is also symmetric against this diagonal. Spectral correlation maps (or simpler "correlation maps") often enable us to observe subtleties in the SC dynamics that are

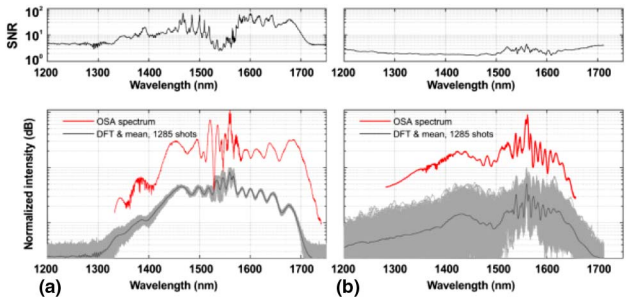

Fig. 10. SNR and the ensembles of DFT single-shot spectra with the averaged spectrum from an OSA before the stretching fiber for the investigated soft glass fibers: (a) NL21 fiber (ANDi) and (b) NL24 fiber (anomalous dispersion) [78].

otherwise impossible to record in ensemble averaging or even in the averaging measurements retaining the phase information [87]. The correlation maps calculated according to Eq. (4) using the experimental data for the NL24 and NL21 fibers are shown in Fig. 11.

The correlation map obtained from experimental data for the NL24 fiber (pumping into anomalous dispersion) [Fig. 11(a)] contains traces typical to soliton dynamics, dominated by SPM, SF, and SSFS, as well as dispersive wave generation. Two correlation maps were calculated for the NL21 fiber. The process of spectral formation, shown in Figs. 11(b) and 11(c), has been shown for two different average pump powers of 350 and 390 mW (with the fiber in-coupling conditions unchanged). The characteristic feature of both maps is the presence of a jitter-like pattern [87]. For the lower pump power (350 mW) [Fig. 11(b)], this pattern can be observed at the red-shifted wavelengths of the spectrum [77], and it appears at the blue-shifted side of the spectrum in the higher pump power recording (390 mW). In both cases these "foot-prints" are assigned to the interaction of FWM and Raman scattering [21]. This pump power-related differentiation of the correlation pattern dynamics can be explained, because the anti-Stokes wing of the Raman scattering signal is usually one to two orders of magnitude less intense than the Stokes-shifted wing. The accompanying process of FWM, in which the higher orders of Raman scattering of the pump pulse act as FWM pump signals, makes the anti-Stokes Raman wing strong enough so that it is only roughly 20%–30% below the level of the Stokes-shifted wing. A clue to the identification of these correlation features can be proposed with the spectral correlation patterns of the pump laser. Its correlation map is shown in Fig. 11(f). Comparing this pattern with the traces present in the long-wavelength and short-wavelength sides of the ANDi spectrum [Figs. 11(d) and 11(e)] suggests a contribution of the pump laser in the SC dynamics. This conclusion may seem trivial, but the correlation map of the laser, shown in Fig. 11(f), was calculated for the laser beam before its coupling into the nonlinear fiber, while the ANDi SC correlation maps were calculated from the data recorded at the output of the nonlinear fiber.

The structure of the NL21 fiber enables propagation of light in the photonic lattice, not only in the core. In fact, this is similar to the double clad fibers known from the fiber laser and fiber amplifier technology. From the point of view of nonlinear optics, it is important to distinguish between the core of the NL21 fiber and its photonic lattice (photonic cladding) with respect to the nonlinear response of the two areas. In the core, the nonlinear processes are supported by strong spatial confinement—that is, by a small effective mode area (see Table 5)—while the photonic lattice has a diameter of about 35 μm. Hence the nonlinear response of the lattice can safely be considered negligible, and the radiation in it is propagated only in a dispersive manner. No nonlinear phase distortion of the pump light takes place. Such an assumption is further supported by linear simulations, which reveal that the lattice supports multiple higher order modes. The electric field of these modes is distributed with different patterns across the lattice, but usually

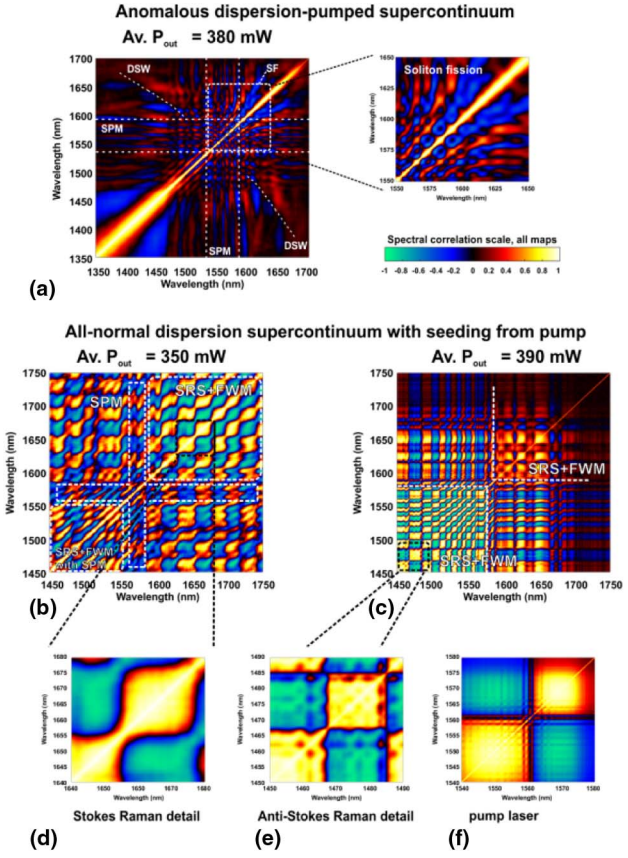

Fig. 11. Spectral correlation maps obtained from DFT measurement data. (a) Typical features of SPM, SF, and calculated location of the dispersive wave (DSW) are indicated for the soliton-based SC. (b), (d) ANDi SC correlation is shown indicating formation of pump-seeded Raman components, first at Stokes-shifted wavelengths (350 mW of average pump power), followed by (c), (e) anti-Stokes-shifted wavelengths (390 mW of average pump power). SRS, stimulated Raman scattering. (f) Spectral correlation of the pump laser is shown in the bottom right [78].

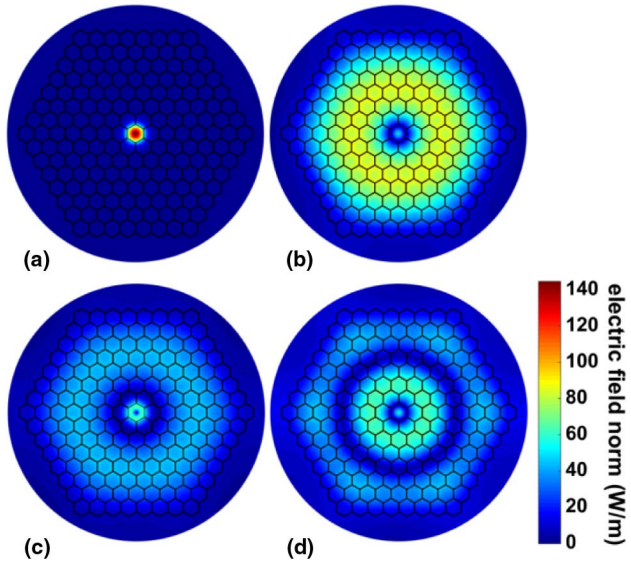

Fig. 12. Numerically obtained mode field distributions. (a) Fundamental mode in the core. (b)–(d) Typical higher order modes in the photonic cladding of the NL21 type ANDi fiber [77,78].

away from the nonlinear core. Still, their overlap with the fundamental mode in the core is non-negligible. Results of these simulations in the form of selected mode distributions—of the fundamental mode in the core and three higher order modes from the photonic cladding—are shown in Fig. 12. During the in-coupling of the pump laser radiation into the core of the NL21 series fibers, a part of the energy excites higher order modes in the lattice. The presence of these modes in the lattice can have an influence on the SC dynamics of the fundamental mode in the fiber core. Specifically, the nonlinearly undisturbed pump laser light (only dispersively stretched) propagated by the lattice around the nonlinear core can deliver a spectral component with a deterministic phase to the core through mode coupling. We note that this coupling mechanism stems from geometric overlap between the core and lattice modes of the discussed all-solid glass ANDi PCFs, and from this point of view it is a linear coupling. This is not to be mistaken with cross-phase modulation, which is a strongly nonlinear process, requiring that both interacting modes experience strong nonlinear response of the waveguide. The deterministic phase component at every step of propagation seeds a four-wave mixing process, pumped by the Raman components, during the spectral broadening in the fiber core. The deterministic seed signal therefore substitutes any possible noise seeds, thus enhancing the phase stability of the SC. Nonlinear propagation simulations could be used to further support this scenario. GNLSE simulations are usually applied to cases limited to the fundamental mode propagation, because the GNLSE is scalar. For this particular case of interaction between a higher order mode from the photonic lattice and the fundamental mode in the core, a vector variant of the GNLSE (MM-GNLSE—multimode GNLSE) has been used. The particular MM-GNLSE model (5) adapted in this study was taken after Refs. [89–91]:

$$
\begin{aligned}
\frac{\partial A_p(z,T)}{\partial z} &= \left[i(\beta_0^{(p)} - \beta_0)A_p(z,T) - (\beta_1^{(p)} - \beta_1)\frac{\partial A_p(z,T)}{\partial T} + i\sum_{n\geq 2}\frac{1}{n!}\beta_n^{(p)}\frac{i^n\partial^n A_p(z,T)}{\partial T^n}\right] \\
&+ \left\{ i\frac{n_2\omega_0}{c}\sum_{l,m,n}\left[\left(1 + i\tau_{\mathrm{plmn}}^{(1)}\frac{\partial}{\partial T}\right)Q_{\mathrm{plmn}}^{(1)}2A_l(z,T)\int R(T')A_m(z,T-T')A_n^*(z,T-T')\mathrm{d}T'\right.\right. \\
&\left.\left. + \left(1 + i\tau_{\mathrm{plmn}}^{(2)}\frac{\partial}{\partial T}\right)Q_{\mathrm{plmn}}^{(2)}2A_l^*(z,T)\int R(T')A_m(z,T-T')A_n(z,T-T')e^{2i\omega_0 T'}\mathrm{d}T'\right]\right\}, \\
Q_{\mathrm{plmn}}^{(1)}(\omega) &= \frac{\varepsilon_0^2 n_0^2 c^2}{12}\frac{\iint[E_p^*(\omega)\cdot E_l(\omega)][E_m(\omega)\cdot E_n^*(\omega)]\mathrm{d}S}{N_p(\omega)N_l(\omega)N_m(\omega)N_n(\omega)}, \\
Q_{\mathrm{plmn}}^{(2)}(\omega) &= \frac{\varepsilon_0^2 n_0^2 c^2}{12}\frac{\iint[E_p^*(\omega)\cdot E_l^*(\omega)][E_m(\omega)\cdot E_n(\omega)]\mathrm{d}S}{N_p(\omega)N_l(\omega)N_m(\omega)N_n(\omega)},
\end{aligned}
\tag{5}
$$

where β_0 is the propagation constant, β_1 is the inverse of the group velocity, β_n denotes the dispersion terms of the two modes, the superscript "(p)" denotes the higher order mode [78], and Q_{plmn} denotes the complex mode coupling coefficients. The remaining symbols are consistent with the scalar GNLSE, where A stands for the complex field amplitude, z is the propagation coordinate, T represents time, n_2 represents the nonlinear refractive index, c represents the speed of light in vacuum, ω_0 represents the center angular frequency of the simulation window (usually also the center frequency of the pump pulse), R represents the delayed Raman response, and τ_{plmn} represents the self-steeping timescale, dependent on the effective mode area.

The numerical load of the MM-GNLSE model is very large and can be prohibitive even on modern, up-to-date computers. For this reason the model was implemented with only the fundamental mode and one single higher order mode from the cladding. The calculations were performed for two cases: (1) using a scalar GNLSE model with only the fundamental mode's chromatic dispersion of the fiber core of the NL21 ANDi fiber, and (2) for the same fiber the MM-GNLSE (vector) model taking into account the fundamental mode and one higher order mode from the photonic lattice. The pump pulse energy considered in the core of the fiber was the same in both types of simulations. It was assumed also that during the in-coupling of pump light into the NL21 fiber 25% of the pulse energy coupled and continued propagation in the photonic cladding, and the remaining 75% coupled and propagated in the core. In order to meet the assumption of equal energies in the fiber core in both simulation series, the total pump pulse energy coupled to the fiber in the vector simulation was accordingly increased. The results are shown in Fig. 13. Four simulations were conducted with each of the models, taking in-coupled pulse energies in the core of 2, 3, 4, and 5 nJ (that is, respectively, 2.85, 4.29, 5.72, and 7.15 nJ total in-coupled energy into the fiber in the vector simulations). SC in the scalar simulation maintains high coherence, however, only for the lower pulse energies, specifically when the spectrum is limited to the self-seeded SPM. As soon as the sidebands begin to appear, noise is amplified across the spectrum, with the long-wavelength part being especially affected, which can be assigned to Raman scattering and has been observed before [92].

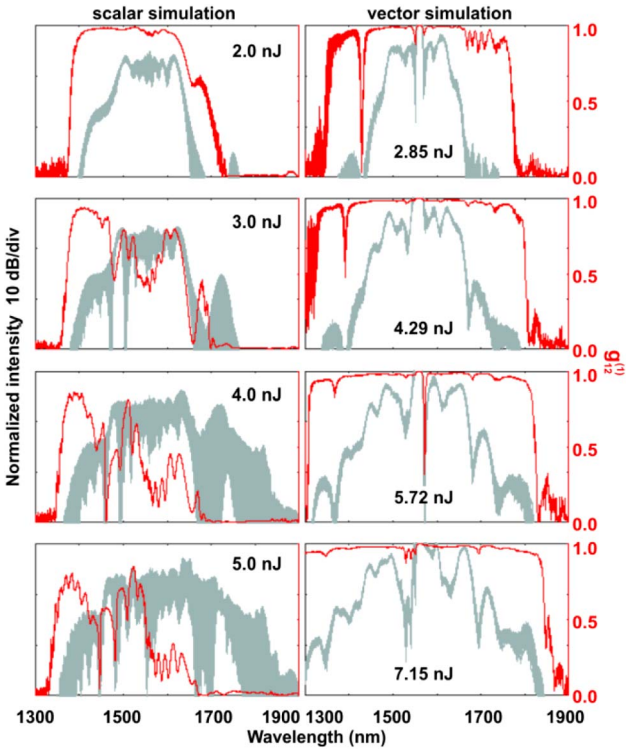

Fig. 13. SC spectra obtained from numerical simulations using modeling (a) scalar GNLSE and (b) two coupled modes (vector) GNLSE. 500-shot realization with one photon per mode noise shown at each plot. In-coupled pump pulse energies shown in each plot [78].

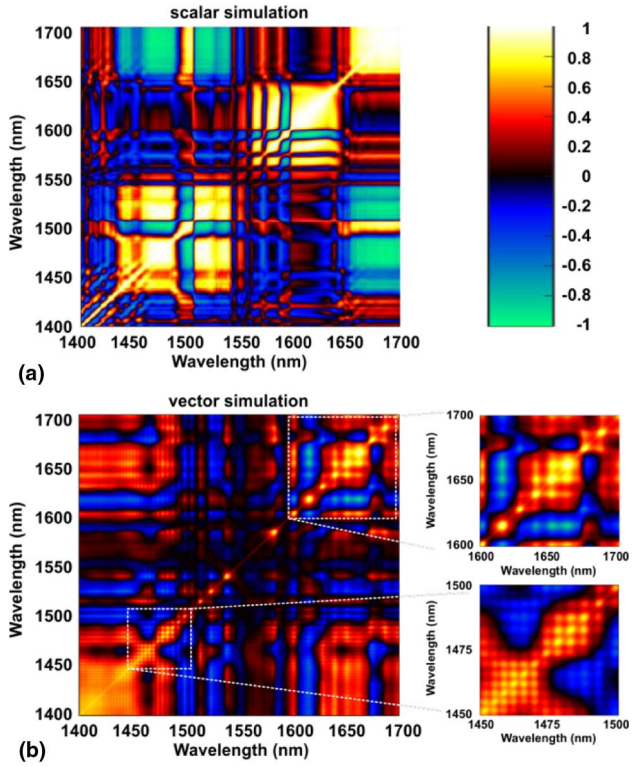

Fig. 14. Spectral correlation maps calculated for the ANDi SC using (a) scalar GNLSE and (b) vector (two coupled modes) GNLSE [78].

As can be seen in the individual plots in Fig. 13(a), the phase fluctuations are accompanied by intensity fluctuations. The SC generated in the vector simulations remains coherent for all investigated pump pulse energies. Specifically, noise amplification is avoided, as in the experiment, even when the spectrum width exceeds SPM.

Correlation maps calculated for the ensembles of simulated spectra (4 and 5.72 nJ pulses for scalar and vector simulations, respectively) differ as well, as shown in Fig. 14. While the map for the scalar simulation data [Fig. 14(a)] clearly shows an area of incoherent Stokes and anti-Stokes wings of FWM-Raman, the vector simulation [Fig. 14(b)] contains a regular structure of correlated spots, located at both the short-wavelength and long-wavelength sides of the spectrum. The pattern in Fig. 14(b) is different than in the maps from the experimental DFT data [Figs. 11(b) and 11(c)], but their common feature is the presence of a rectangular grid structure of correlated areas. The vector simulation included only one mode from the photonic cladding, which could be delivering the deterministic seed signal. The real fiber structure simultaneously supports multiple higher order modes with an overlap to the core. The correlation pattern obtained from experimental data [Figs. 11(b) and 11(c)] is therefore a result of a spatio-temporal average of influence of many modes with different dispersion characteristics and different group velocity mismatch with the core mode, and that interact with the core mode at different fragments of propagation along the fiber, with different mode couplings.

7. NANOSTRUCTURING OF FIBER CORE AS NEW MEANS OF DISPERSION AND EFFECTIVE MODE AREA ENGINEERING

The recent results, in particular the comparison of the NL21 and NL38 series ANDi PCFs in pulse-preserving SC performance, suggest a significant influence of the engineering of the effective mode area dependence on wavelength, on par with dispersion engineering. The changes of both characteristics due to the manipulation of the transverse geometry of the fiber structure are strongly related. This can be a limitation in the designing of a nonlinear fiber for ANDi SC generation. Moreover, there is a limited number of glass compositions with a satisfactory refractive index contrast, which enable joint thermal processing into all-solid glass structured fibers.

The ITME glass and optical fiber group recently reported a world-first nanostructured core, graded-index optical fiber [93]. The core of the fiber was composed of about 8000 glass rods from two types of boron-silicate glasses with refractive indices of $n_D = 1.5273$ and $n_D = 1.5581$. The technological approach was based on the effective medium theorem. Here the refractive index distribution experienced by the wave propagated in the structure stems from an effective value of refractive index shaped by the distribution of the structure's constituent elements, as long as these elements are sub-wavelength in size. The team designed the distribution profile of the elements in the structure according to the desired parabolic profile of the refractive index. The structure topology and theoretical refractive index profile are shown in Figs. 15(a) and 15(b). The stacked fiber core preform is shown in Fig. 15(c). It was 6 cm

Table 6. Geometrical Parameters of the Fabricated Nanostructured Core Fibers [93]

No	Outer Diameter [μm]	Core Dimensions [μm × μm]
1	74.2	6.9 × 6.0
2	58.5	5.4 × 4.9
3	122.2	4.0 × 4.4
4	110.3	3.7 × 4.2
5	100.9	3.3 × 3.9
6	90.16	2.8 × 3.2

long at the longer diagonal, and a single rod was 0.6 mm in diameter. The long diagonal contains exactly 100 rods. After a first drawing step in a fiber drawing tower, the preform had a diameter of about 2.5 mm (depending on a particular sample and intended follow-up processing) [Fig. 15(d)]. Before drawing into the final fiber, this sub-preform was placed in a lower-refractive index glass tube. The series of drawn optical fibers comprised several samples with different diameters of the nanostructured core, ranging from about 3 to 7 μm. The outer diameters were in the range of 74 to 120 μm and depended on the process conditions. Their variation from sample to sample did not influence the dispersive properties of the fibers. The geometrical parameters of the fabricated fibers are presented in Table 6, and the SEM images of selected final fibers are shown in Figs. 15(e) and 15(f).

The refractive index profile in the fabricated fibers was symmetric against the axis of the fiber, but it is possible to create other, asymmetric topologies of gradient index fibers using the same technological platform. In the fabricated test series of fibers, the dispersion profile followed a reversed trend of evolution with changes of the core dimension to what is known from the existing literature. The zero-dispersion point was red-shifting and then disappearing altogether (the dispersion profile moving into the all-normal range of values—within the studied wavelength range) along with decreasing of the core diameter, as shown in Figs. 16(a) and 16(b). Results of energy-dispersive X-ray spectroscopy (EDS) measurements on the fiber samples revealed a process of selective diffusion of certain atoms of the chemical composition of the core glasses. As a result, the spatial profiles of distribution of atoms including barium, silicon, and oxygen in the boron-silicate glasses are changed at the nanostructure level, compared to the drawn preform of the core. A further consequence is that in the final fiber there is a change of the material dispersion contribution of the nanostructure in the core. This hypothesis is confirmed by numerical simulations, in which the material dispersion profile was modified within the nanostructured core area. Using one such optimized material dispersion profile allowed the numerical reconstruction of both the initially assumed parabolic distribution of the refractive index profile (shaped primarily by the barium atom concentration) and the trend of evolution of the fiber dispersion with the change of the nanostructured core dimension. These results are shown in Figs. 16(c) and 16(d).

This demonstration shows that the traditional tradeoff between effective nonlinearity and flatness of the chromatic dispersion profile might be overcome by novel nanostructures in the core region of the fiber. The experimental demonstration

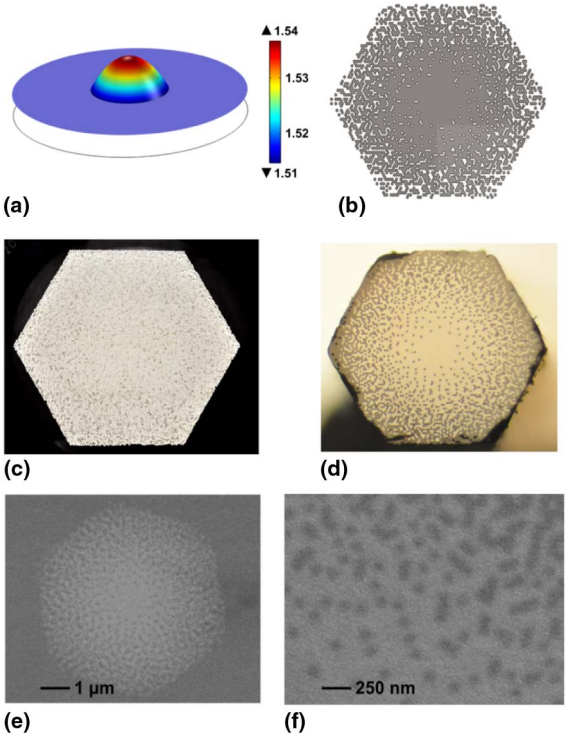

Fig. 15. (a) Design of the core nanostructure, (b) theoretical distribution of the refractive index in the core, (c) stacked preform of fiber core, and (d) core preform drawn at a fiber drawing tower. Typical SEM images of (e) final nanostructured core fiber-core area and (f) detail of the core nanostructure [93].

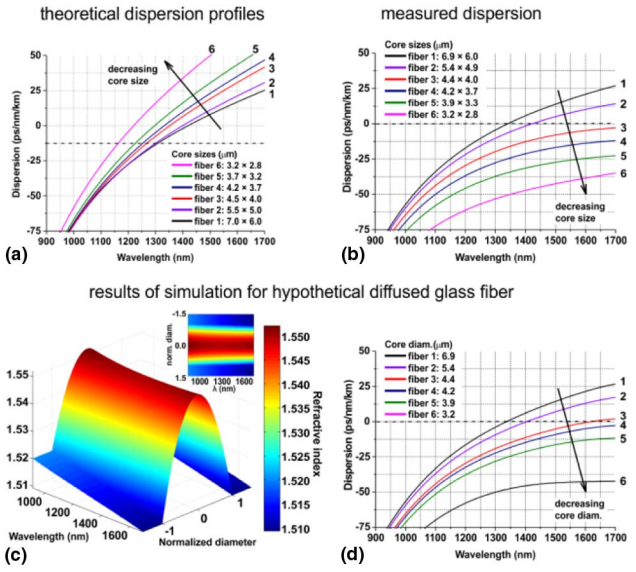

Fig. 16. (a) Chromatic dispersion estimated from the design of the nanostructured core fibers based on numerical simulations. (b) Measured dispersion profiles of the fabricated fibers. (c) Spatial and spectral profile of the effective refractive index in the nanostructured core (dependence on the normalized diameter). (d) Chromatic dispersion profiles calculated for the fibers with different core diameters for an optimized material dispersion at the core nanostructure level [93].

of refractive index profile shaping in an arbitrary manner, which was constrained neither to any axial symmetry nor to any other limitations known from the gradient index fiber technology, is a first step in this direction. In the context of ANDi SC generation the design of normal dispersion profiles with robust core sizes facilitating strong nonlinear response of the nanostructured fiber would be of interest. At the same time, nonlinear mode self-cleanup, reported in standard multimode graded-index fibers [94], could offer yet new solutions to manage the mode structure of this type of ANDi fibers, answering the concerns about the expected multimode operation inherent to strongly confining fiber cores.

8. CONCLUSIONS

Advancements in femtosecond laser technology improve the accessibility to coherent, broadband light sources. This is further fortified by new developments in nonlinear optical fibers. High-quality, octave-spanning, and pulse-preserving SC laser setups have been reported in silica, silicate, and chalcogenide glass fibers, at wavelength ranges covering the spectral region from the UV up to 5 μm. In particular, with maturing of the ytterbium and erbium fiber-based femtosecond lasers (1.06 and 1.56 μm) and with the rapid progress in thulium or thulium-holmium co-doped femtosecond systems (1.9–2.1 μm), the entire near-infrared from about 0.7 to 2.8 μm can be covered with a single pulse-preserving SC using reliable silica or silicate ANDi PCFs. Extending this coverage into the mid-infrared over the 2.8–3.2 μm OH^- edge of silica or silicate glasses requires non-oxide glass fibers. While potential candidates include standard step-index chalcogenide fibers, the required pump wavelength is located in the mid-infrared, and currently is available only from complex OPA systems. From the application point of view, pulse-preserving SC in the near-infrared is very attractive since its bandwidth matches amplification bands of the three robust fiber amplifier systems based on ytterbium, erbium, and thulium dopant ions, enabling interesting possibilities in power scaling of high-quality, ultra-short light pulses in relatively compact setups.

We have summarized the design, characteristics, and SC generation performance in all-solid soft glass PCFs. Results obtained with fibers on this glass platform remain generally compatible with silica or silica–germanium fibers with the attainable spectral band reaching out to about 2.2–2.4 μm with 1.56 μm femtosecond pumping. Comparative studies performed with two families of soft glass ANDi fibers pumped at wavelengths exceeding 2.0 μm suggest that the ANDi SC bandwidth is significantly influenced by the strength of the effective nonlinearity, a factor that can be influenced to a large extent by the choice of glass composition. This gives an additional degree of design freedom in comparison to silica fibers, where the SC bandwidth is usually determined by the flatness of the ANDi dispersion profile.

Decoherence of normal dispersion-pumped SC pulses with increasing pump pulse duration is an issue if means of softening the requirements on the pump pulse parameters—and thus the complexity of the pump source—should be considered. We have experimentally compared the phase coherence and spectral stability of solitonic, MI-driven SC and of an ANDi SC. Coherence enhancement in the ANDi SC has been theoretically investigated using numerical modeling, supported by spectral correlation maps calculated from measured shot-to-shot resolved spectra. The suggested mechanism has been assigned to the interaction between the fundamental mode of the PCF core and the higher order modes from the surrounding photonic lattice. It is suggested that in this specific case of ANDi PCF, where the lattice area supports index guiding, the lattice modes deterministically seed the nonlinear process in the core, mitigating any possible noise amplification effects. The spatio-temporal approach to modification of the stochastic properties of SC can be further exploited in nanostructured graded-index core fibers, in which the mode areas and dispersion profiles can be shaped by arbitrary designs of the refractive index profiles. We have demonstrated nanostructured core graded-index fibers using the silicate glass platform, although the approach principally based on the standard stack-and-draw procedure should be fully compatible with the silica and non-oxide glasses as well.

The review contained in this work allows us to conclude that in terms of further extending the spectrum of pulse-preserving SC, the fiber material choices are practically exhausted. In the near-infrared wavelengths, the silica or silicate glass fibers enable covering wavelengths up to 2.8 μm under pumping with standard femtosecond lasers. Extending the spectrum further beyond the OH^- absorption band at this wavelength requires a different glass. An immediate solution is available even with a commercial mid-infrared fiber patchcord, but the required femtosecond pump laser wavelength is currently obtainable only from a complex parametric amplifier source [37]. Therefore from the fiber design perspective, it would be desirable to obtain fibers with normal dispersion profiles and mode area characteristics engineered for efficient cascading of ANDi fibers. Thus the cascade would begin with an ANDi PCF suitable for pumping with a mature femtosecond laser operating at either 1.0 or 1.56 μm and then continue extension of the spectrum in a following cascade stage constituted by, e.g., a fluoride, tellurite, or chalcogenide fiber. This approach has already been validated for the MI-driven, anomalous dispersion SC [95].

While it cannot be reasonably expected that ANDi SC would exceed solitonic, MI-driven sources in terms of bandwidth for comparable pump powers, the noise suppression property—in the fiber-based broadband sources unique to ANDi SC—is the central property for a number of exciting applications in photonics. In particular, the spectral compatibility of near-infrared ANDi SC with robust fiber amplifiers and the associated opportunity of power scalability for high-quality, intrinsically synchronized ultra-short coherent light pulses makes for a convenient starting point for extending spectral coverage into the mid-infrared. Such extension in the case of phase-coherent SC would further serve many applications, e.g., in the field of photochemistry pump-probe spectroscopy, which presently require complex non-collinear optical parametric amplifier (NOPA) systems.

Funding. Fundacja na rzecz Nauki Polskiej (FNP) (First TEAM/2016-1/1).

Acknowledgment. This work has been carried out in scope of the project "High temporal quality ultrashort pulse generation for coherent seeding of high power near- and mid-infrared optical amplifiers" realized within the First TEAM programme of the Foundation for Polish Science co-financed by the European Union under the European Regional Development Fund.

REFERENCES

1. S. Ishida and N. Nishizawa, "Quantitative comparison of contrast and imaging depth of ultrahigh-resolution optical coherence tomography images in 800-1700 nm wavelength region," Biomed. Opt. Express **3**, 282–294 (2012).
2. Y. Takushima and K. Kikuchi, "10-GHz over 20-channel multiwavelength pulse source by slicing super-continuum spectrum generated in normal-dispersion fiber," IEEE Photon. Technol. Lett. **11**, 322–324 (1999).
3. Y. Sun, C. F. Booker, S. Kumari, R. N. Day, M. Davidson, and A. Periasamy, "Characterization of an orange acceptor fluorescent protein for sensitized spectral fluorescence resonance energy transfer microscopy using a white-light laser," J. Biomed. Opt. **14**, 054009 (2009).
4. U. Sharma, E. W. Chang, and S. H. Yun, "Long-wavelength optical coherence tomography at 1.7 μm for enhanced imaging depth," Opt. Express **16**, 19712–19723 (2008).
5. H. Kawagoe, S. Ishida, M. Aramaki, Y. Sakakibara, E. Omoda, H. Kataura, and N. Nishizawa, "Development of a high power supercontinuum source in the 1.7 μm wavelength region for highly penetrative ultrahigh-resolution optical coherence tomography," Biomed. Opt. Express **5**, 932–943 (2014).
6. C. S. Cheung, J. M. O. Daniel, M. Tokurakawa, W. A. Clarkson, and H. Liang, "High resolution Fourier domain optical coherence tomography in the 2 μm wavelength range using a broadband supercontinuum source," Opt. Express **23**, 1992–2001 (2015).
7. R. Wu, V. T. Company, D. E. Leaird, and A. M. Weiner, "Supercontinuum-based 10-GHz flat-topped optical frequency comb generation," Opt. Express **21**, 6045–6052 (2013).
8. C.-B. Huang, S.-G. Park, D. E. Leaird, and A. M. Weiner, "Nonlinearly broadened phase-modulated continuous-wave laser frequency combs characterized using DPSK decoding," Opt. Express **16**, 2520–2527 (2008).
9. A. Sihvola, *Electromagnetic Mixing Formulas and Applications* (Institution of Electrical Engeneers, 1999).
10. R. R. Alfano and S. L. Shapiro, "Emission in the region 4000 to 7000 Å via four-photon coupling in glass," Phys. Rev. Lett. **24**, 584–587 (1970).
11. J. M. Dudley, G. Genty, and S. Coen, "Supercontinuum generation in photonic crystal fiber," Rev. Mod. Phys. **78**, 1135–1184 (2006).
12. J. K. Ranka, R. S. Windeler, and A. J. Stentz, "Visible continuum generation in air-silica microstructure optical fibers with anomalous dispersion at 800 nm," Opt. Lett. **25**, 25–27 (2000).
13. J. M. Dudley and S. Coen, "Coherence properties of supercontinuum spectra generated in photonic crystal and tapered optical fibers," Opt. Lett. **27**, 1180–1182 (2002).
14. R. H. Stolen, J. P. Gordon, W. J. Tomlinson, and H. A. Haus, "Raman response function of silica-core fibers," J. Opt. Soc. Am. B **6**, 1159–1166 (1989).
15. P. Domachuk, N. A. Wolchover, M. Cronin-Golomb, A. Wang, A. K. George, C. M. B. Cordeiro, J. C. Knight, and F. G. Omenetto, "Over 4000 nm bandwidth of mid-IR supercontinuum generation in sub-centimeter segments of highly nonlinear tellurite PCFs," Opt. Express **16**, 7161–7168 (2008).
16. C. Agger, C. Petersen, S. Dupont, H. Steffensen, J. K. Lyngsø, C. L. Thomsen, J. Thøgersen, S. R. Keiding, and O. Bang, "Supercontinuum generation in ZBLAN fibers—detailed comparison between measurement and simulation," J. Opt. Soc. Am. B **29**, 635–645 (2012).
17. C. R. Petersen, U. Møller, I. Kubat, B. Zhou, S. Dupont, J. Ramsay, T. Benson, S. Sujecki, N. Abdel-Moneim, Z. Tang, D. Furniss, A. Seddon, and O. Bang, "Mid-infrared supercontinuum covering the 1.4-13.3 μm molecular fingerprint region using ultra-high NA chalcogenide step-index fibre," Nat. Photonics **8**, 830–834 (2014).
18. G. Sobon, M. Klimczak, J. Sotor, K. Krzempek, D. Pysz, R. Stepien, T. Martynkien, K. M. Abramski, and R. Buczynski, "Infrared supercontinuum generation in softglass photonic crystal fibers pumped at 1560 nm," Opt. Mat. Express **4**, 7–15 (2014).
19. M. Klimczak, B. Siwicki, P. Skibinski, D. Pysz, R. Stepien, A. Szolno, J. Pniewski, C. Radzewicz, and R. Buczynski, "Mid-infrared supercontinuum generation in soft-glass suspended core photonic crystal fiber," Opt. Quantum Electron. **46**, 563–571 (2014).
20. M. Klimczak, G. Stepniewski, H. Bookey, A. Szolno, R. Stepien, D. Pysz, A. Kar, A. Waddie, M. R. Taghizadeh, and R. Buczynski, "Broadband infrared supercontinuum generation in hexagonal-lattice tellurite photonic crystal fiber with dispersion optimized for pumping near 1560 nm," Opt. Lett. **38**, 4679–4682 (2013).
21. G. P. Agrawal, *Nonlinear Fiber Optics*, 3rd ed. (Academic, 2001).
22. T. Godin, Y. Combes, R. Ahmad, M. Rochette, T. Sylvestre, and J. M. Dudley, "Far-detuned mid-infrared frequency conversion via normal dispersion modulation instability in chalcogenide microwires," Opt. Lett. **39**, 1885–1888 (2014).
23. U. Møller and O. Bang, "Intensity noise in normal-pumped picoseconds supercontinuum generation, where higher-order Raman lines cross into the anomalous dispersion regime," Electron. Lett. **49**, 63–65 (2013).
24. S. R. Domingue and R. A. Bartels, "Overcoming temporal polarization instabilities from the latent birefringence in all-normal dispersion, wave-breaking-extended nonlinear fiber supercontinuum generation," Opt. Express **21**, 13305–13321 (2013).
25. Y. Liu, Y. Zhao, J. Lyngsø, S. You, W. L. Wilson, H. Tu, and S. A. Boppart, "Suppressing short-term polarization noise and related spectral decoherence in all-normal dispersion fiber supercontinuum generation," J. Lightwave Technol. **33**, 1814–1820 (2015).
26. S. T. Sørensen, C. Larsen, U. Møller, P. M. Moselund, C. L. Thomsen, and O. Bang, "The role of phase coherence in seeded supercontinuum generation," Opt. Express **20**, 22886–22894 (2012).
27. D. M. Nguyen, T. Godin, S. Toenger, Y. Combes, B. Wetzel, T. Sylvestre, J.-M. Merolla, L. Larger, G. Genty, F. Dias, and J. M. Dudley, "Incoherent resonant seeding of modulation instability in optical fiber," Opt. Lett. **38**, 5338–5341 (2013).
28. Z. Ren, Y. Xu, Y. Qiu, K. K. Y. Wong, and K. Tsia, "Spectrally-resolved statistical characterization of seeded supercontinuum suppression using optical time-stretch," Opt. Express **22**, 11849–11860 (2014).
29. P. Falk, M. H. Frosz, and O. Bang, "Supercontinuum generation in a photonic crystal fiber with two zero-dispersion wavelengths tapered to normal dispersion at all wavelengths," Opt. Express **13**, 7535–7540 (2005).
30. F. Li, Q. Li, J. Yuan, and P. K. A. Wai, "Highly coherent supercontinuum generation with picosecond pulses by using self-similar compression," Opt. Express **22**, 27339–27354 (2014).
31. L. E. Hooper, P. J. Mosley, A. C. Muir, W. J. Wadsworth, and J. C. Knight, "Coherent supercontinuum generation in photonic crystal fiber with all-normal group velocity dispersion," Opt. Express **19**, 4902–4907 (2011).
32. A. M. Heidt, A. Hartung, G. W. Bosman, P. Krok, E. G. Rohwer, H. Schwoerer, and H. Bartelt, "Coherent octave spanning near-infrared and visible supercontinuum generation in all-normal dispersion photonic crystal fibers," Opt. Express **19**, 3775–3787 (2011).
33. N. Nishizawa and J. Takayanagi, "Octave spanning high-quality supercontinuum generation in all-fiber system," J. Opt. Soc. Am. B **24**, 1786–1792 (2007).
34. K. Chow, Y. Takushima, C. Lin, C. Shu, and A. Bjarklev, "Flat supercontinuum generation based on normal dispersion nonlinear photonic crystal fiber," Electron. Lett. **42**, 989–990 (2006).
35. M. Klimczak, B. Siwicki, B. Zhou, M. Bache, D. Pysz, O. Bang, and R. Buczyński, "Coherent supercontinuum bandwidth limitations under femtosecond pumping at 2 μm in all-solid soft glass photonic crystal fibers," Opt. Express **24**, 29406–29416 (2016).

36. K. Tarnowski, T. Martynkien, P. Mergo, K. Poturaj, G. Soboń, and W. Urbańczyk, "Coherent supercontinuum generation up to 2.2 μm in an all-normal dispersion microstructured silica fiber," Opt. Express **24**, 30523–30536 (2016).
37. S. Kedenburg, T. Steinle, F. Mörz, A. Steinmann, and H. Giessen, "High-power mid-infrared high repetition-rate supercontinuum source based on a chalcogenide step-index fiber," Opt. Lett. **40**, 2668–2671 (2015).
38. X. Li, W. Chen, T. Xue, J. Gao, W. Gao, L. Hu, and M. Liao, "Low threshold mid-infrared supercontinuum generation in short fluoride-chalcogenide multimaterial fibers," Opt. Express **22**, 24179–24191 (2014).
39. L. Liu, T. Cheng, K. Nagasaka, H. Tong, G. Qin, T. Suzuki, and Y. Ohishi, "Coherent mid-infrared supercontinuum generation in all-solid chalcogenide microstructured fibers with all-normal dispersion," Opt. Lett. **41**, 392–395 (2016).
40. A. R. Johnson, A. S. Mayer, A. Klenner, K. Luke, E. S. Lamb, M. R. E. Lamont, C. Joshi, Y. Okawachi, F. W. Wise, M. Lipson, U. Keller, and A. L. Gaeta, "Octave-spanning coherent supercontinuum generation in a silicon nitride waveguide," Opt. Lett. **40**, 5117–5120 (2015).
41. R. Salem, Z. Jiang, D. Liu, R. Pafchek, D. Gardner, P. Foy, M. Saad, D. Jenkins, A. Cable, and P. Fendel, "Mid-infrared supercontinuum generation spanning 1.8 octaves using step-index indium fluoride fiber pumped by a femtosecond fiber laser near 2 μm," Opt. Express **23**, 30592–30602 (2015).
42. A. M. Heidt, J. Rothhardt, A. Hartung, H. Bartelt, E. G. Rohwer, J. Limpert, and A. Tünnermann, "High quality sub-two cycle pulses from compression of supercontinuum generated in all-normal dispersion photonic crystal fiber," Opt. Express **19**, 13873–13879 (2011).
43. S. Demmler, J. Rothhardt, A. M. Heidt, A. Hartung, E. G. Rohwer, H. Bartelt, J. Limpert, and A. Tünnermann, "Generation of high quality, 1.3 cycle pulses by active phase control of an octave spanning supercontinuum," Opt. Express **19**, 20151–20158 (2011).
44. J. Rothhardt, S. Demmler, S. Hädrich, J. Limpert, and A. Tünnermann, "Octave-spanning OPCPA system delivering CEP-stable few-cycle pulses and 22 W of average power at 1 MHz repetition rate," Opt. Express **20**, 10870–10878 (2012).
45. M. Cassataro, D. Novoa, M. C. Günendi, N. N. Edavalath, M. H. Frosz, J. C. Travers, and P. St. J. Russell, "Generation of broadband mid-IR and UV light in gas-filled single-ring hollow-core PCF," Opt. Express **25**, 7637–7644 (2017).
46. S. Kedenburg, T. Gissibl, T. Steinle, A. Steinmann, and H. Giessen, "Towards integration of a liquid-filled fiber capillary for supercontinuum generation in the 1.2-2.4 μm range," Opt. Express **23**, 8281–8289 (2015).
47. X. Feng, T. M. Monro, P. Petropoulos, V. Finazzi, and D. Hewak, "Solid microstructured optical fiber," Opt. Express **11**, 2225–2230 (2003).
48. R. Buczyński, J. Pniewski, D. Pysz, R. Stępień, R. Kasztelanic, I. Kujawa, A. Filipkowski, A. J. Waddie, and M. R. Taghizadeh, "Dispersion management in soft glass all-solid photonic crystal fibres," Optoelectron. Rev. **20**, 207–215 (2012).
49. D. Lorenc, M. Aranyosiova, R. Buczynski, R. Stepien, I. Bugar, A. Vincze, and D. Velic, "Nonlinear refractive index of multicomponent glasses designed for fabrication of photonic crystal fibers," Appl. Phys. B **93**, 531–538 (2008).
50. V. L. Kalashnikov, E. Sorokin, and I. T. Sorokina, "Raman effects in the infrared supercontinuum generation in soft-glass PCFs," Appl. Phys. B **87**, 37–44 (2007).
51. A. M. Heidt, "Pulse preserving flat-top supercontinuum generation in all-normal dispersion photonic crystal fibers," J. Opt. Soc. Am. B **27**, 550–559 (2010).
52. A. M. Heidt, A. Hartung, and H. Bartelt, "Generation of ultrashort and coherent supercontinuum light pulses in all-normal dispersion fibers," in The Supercontinuum Laser Source, R. Alfano, ed. (Springer, 2016), pp. 247–280.
53. G. Stepniewski, M. Klimczak, H. Bookey, B. Siwicki, D. Pysz, R. Stepien, A. K. Kar, A. J. Waddie, M. R. Taghizadeh, and R. Buczynski, "Broadband supercontinuum generation in normal dispersion all-solid photonic crystal fiber pumped near 1300 nm," Laser Phys. Lett. **11**, 055103 (2014).
54. M. Klimczak, B. Siwicki, P. Skibiński, D. Pysz, R. Stępień, A. Heidt, C. Radzewicz, and R. Buczyński, "Coherent supercontinuum generation up to 2.3 μm in all-solid soft-glass photonic crystal fibers with flat all-normal dispersion," Opt. Express **22**, 18824–18832 (2014).
55. T. Cheng, K. Nagasaka, T. H. Tuan, X. Xue, M. Matsumoto, H. Tezuka, T. Suzuki, and Y. Ohishi, "Mid-infrared supercontinuum generation spanning 2.0 to 15.1 μm in a chalcogenide step-index fiber," Opt. Lett. **41**, 2117–2120 (2016).
56. O. Mouawad, P. Béjot, F. Billard, P. Mathey, B. Kibler, F. Désévédavy, G. Gadret, J.-C. Jules, O. Faucher, and F. Smektala, "Mid-infrared filamentation-induced supercontinuum in As-S and an As-free Ge-S counterpart chalcogenide glasses," Appl. Phys. B **121**, 433–438 (2015).
57. T. Cheng, W. Gao, M. Liao, Z. Duan, D. Deng, M. Matsumoto, T. Misumi, T. Suzuki, and Y. Ohishi, "Tunable third-harmonic generation in a chalcogenide-tellurite hybrid optical fiber with high refractive index difference," Opt. Lett. **39**, 1005–1007 (2014).
58. M. Liao, W. Gao, T. Cheng, Z. Duan, X. Xue, T. Suzuki, and Y. Ohishi, "Flat and broadband supercontinuum generation by four-wave mixing in a highly nonlinear tapered microstructured fiber," Opt. Express **20**, B574–B580 (2012).
59. J. Picot-Clemente, C. Strutynski, F. Amrani, F. Désévédavy, J.-C. Jules, G. Gadret, D. Deng, T. Cheng, K. Nagasaka, Y. Ohishi, B. Kibler, and F. Smektala, "Enhanced supercontinuum generation in tapered tellurite suspended core fiber," Opt. Commun. **354**, 374–379 (2015).
60. C. Strutynski, P. Froidevaux, F. Désévédavy, J.-C. Jules, G. Gadret, A. Bendahmane, K. Tarnowski, B. Kibler, and F. Smektala, "Tailoring supercontinuum generation beyond 2 μm in step-index tellurite fibers," Opt. Lett. **42**, 247–250 (2017).
61. S. Kedenburg, C. Strutynski, B. Kibler, P. Froidevaux, F. Désévédavy, G. Gadret, J.-C. Jules, T. Steinle, F. Morz, A. Steinmann, H. Giessen, and F. Smektala, "High repetition rate mid-infrared supercontinuum generation from 1.3 to 5.3 μm in robust step-index tellurite fibers," J. Opt. Soc. Am. B **34**, 601–607 (2017).
62. T. H. Tuan, T. Cheng, K. Asano, Z. Duan, W. Gao, D. Deng, T. Suzuki, and Y. Ohishi, "Optical parametric gain and bandwidth in highly nonlinear tellurite hybrid microstructured optical fiber with four zero-dispersion wavelengths," Opt. Express **21**, 20303–20312 (2013).
63. C. Strutynski, F. Desevedavy, A. Lemière, J.-C. Jules, G. Gadret, T. Cardinal, F. Smektala, and S. Danto, "Tellurite-based core-clad dual-electrodes composite fibers," Opt. Mater. Express **7**, 1503–1508 (2017).
64. C. Xia, M. Kumar, O. P. Kulkarni, M. N. Islam, F. L. Terry, Jr., M. J. Freeman, M. Poulain, and G. Maze, "Mid-infrared supercontinuum generation to 4.5 μm in ZBLAN fluoride fibers by nanosecond diode pumping," Opt. Lett. **31**, 2553–2555 (2006).
65. A. M. Heidt, J. H. V. Price, C. Baskiotis, J. S. Feehan, Z. Li, S. U. Alam, and D. J. Richardson, "Mid-infrared ZBLAN fiber supercontinuum source using picosecond diode-pumping at 2 μm," Opt. Express **21**, 24281–24287 (2013).
66. X. Jiang, N. Y. Joly, M. A. Finger, F. Babic, G. K. L. Wong, J. C. Travers, and P. St. J. Russell, "Deep-ultraviolet to mid-infrared supercontinuum generated in solid-core ZBLAN photonic crystal fibre," Nat. Photonics **9**, 133–139 (2015).
67. NKT Photonics, http://www.nktphotonics.com; LEUKOS, http://www.leukos-systems.com, Le Verre Fluoré, http://leverrefluore.com/, Thorlabs, http://www.thorlabs.com.
68. A. Hartung, A. M. Heidt, and H. Bartelt, "Pulse-preserving broadband visible supercontinuum generation in all-normal dispersion tapered suspended-core optical fibers," Opt. Express **19**, 12275–12283 (2011).
69. H. Sotobayashi and K. Kitayama, "325 nm bandwidth supercontinuum generation at 10 Gbit/s using dispersion-flattened and non-decreasing normal dispersion fibre with pulse compression technique," Electron. Lett. **34**, 1336–1337 (1998).
70. I. A. Sukhoivanov, S. O. Iakushev, O. V. Shulika, E. Silvestre, and M. V. Andres, "Design of all-normal dispersion microstructured optical fiber on silica platform for generation of pulse-preserving supercontinuum under excitation at 1550 nm," J. Lightwave Technol. **35**, 3772–3779 (2017).

71. C. C. Wang, M. H. Wang, and J. Wu, "Heavily germanium-doped silica fiber with a fat normal dispersion profile," IEEE Photon. J. **7**, 7101110 (2015).
72. K. Tarnowski and W. Urbanczyk, "All-normal dispersion hole-assisted silica fibers for generation of supercontinuum reaching midinfrared," IEEE Photon. J. **8**, 7100311 (2016).
73. A. M. Heidt, Z. Li, and D. J. Richardson, "High power diode-seeded fiber amplifiers at 2 μm—from architectures to applications," IEEE J. Sel. Top. Quantum Electron. **20**, 3100612 (2014).
74. J. Sotor, G. Sobon, M. Kowalczyk, W. Macherzynski, P. Paletko, and K. M. Abramski, "Ultrafast thulium-doped fiber laser mode locked with black phosphorus," Opt. Lett. **40**, 3885–3888 (2015).
75. H. Tu, Y. Liu, X. Liu, D. Turchinovich, J. Lægsgaard, and S. A. Boppart, "Nonlinear polarization dynamics in a weakly birefringent all-normal dispersion photonic crystal fiber: toward a practical coherent fiber supercontinuum laser," Opt. Express **20**, 1113–1128 (2012).
76. T. Martynkien, D. Pysz, R. Stępień, and R. Buczyński, "All-solid microstructured fiber with flat normal chromatic dispersion," Opt. Lett. **39**, 2342–2345 (2014).
77. M. Klimczak, G. Soboń, K. M. Abramski, and R. Buczyński, "Spectral coherence in all-normal dispersion supercontinuum in presence of Raman scattering and direct seeding from sub-picosecond pump," Opt. Express **22**, 31635–31645 (2014).
78. M. Klimczak, G. Soboń, R. Kasztelanic, K. M. Abramski, and R. Buczyński, "Direct comparison of shot-to-shot noise performance of all normal dispersion and anomalous dispersion supercontinuum pumped with sub-picosecond pulse fiber-based laser," Sci. Rep. **6**, 19284 (2016).
79. J. Sotor, M. Pawliszewska, G. Sobon, P. Kaczmarek, A. Przewolka, I. Pasternak, J. Cajzl, P. Peterka, P. Honzátko, I. Kašík, W. Strupinski, and K. M. Abramski, "All-fiber Ho-doped mode-locked oscillator based on a graphene saturable absorber," Opt. Lett. **41**, 2592–2595 (2016).
80. Q. Wang, J. Geng, Z. Jiang, T. Luo, and S. Jiang, "Mode-locked Tm-Ho-codoped fiber laser at 2.06 μm," IEEE Photon. Technol. Lett. **23**, 682–684 (2011).
81. B. Siwicki, R. Kasztelanic, M. Klimczak, J. Cimek, D. Pysz, R. Stępień, and R. Buczyński, "Extending of flat normal dispersion profile in all-solid soft glass nonlinear photonic crystal fibres," J. Opt. **18**, 065102 (2016).
82. A. M. Heidt, J. S. Feehan, J. H. V. Price, and T. Feurer, "Limits of coherent supercontinuum generation in normal dispersion fibers," J. Opt. Soc. Am. B **34**, 764–775 (2017).
83. J. M. Dudley and J. R. Taylor, eds., *Supercontinuum Generation in Optical Fibers* (Cambridge, 2010).
84. S. Coen, A. H. L. Chau, R. Leonhardt, J. D. Harvey, J. C. Knight, W. J. Wadsworth, and P. St. J. Russell, "Supercontinuum generation by stimulated Raman scattering and parametric four-wave mixing in photonic crystal fibers," J. Opt. Soc. Am. B **19**, 753–764 (2002).
85. G. Sobon, "Mode-locking of fiber lasers using novel two-dimensional nanomaterials: graphene and topological insulators," Photon. Res. **3**, A56–A63 (2015).
86. K. Goda and B. Jalali, "Dispersive Fourier transformation for fast continuous single-shot measurements," Nat. Photonics **7**, 102–112 (2013).
87. B. Wetzel, A. Stefani, L. Larger, P. A. Lacourt, J. M. Merolla, T. Sylvestre, A. Kudlinski, A. Mussot, G. Genty, F. Dias, and J. M. Dudley, "Real-time full bandwidth measurement of spectral noise in supercontinuum generation," Sci. Rep. **2**, 882 (2012).
88. T. Godin, B. Wetzel, T. Sylvestre, L. Larger, A. Kudlinski, A. Mussot, A. Ben Salem, M. Zghal, G. Genty, F. Dias, and J. M. Dudley, "Real time noise and wavelength correlations in octave-spanning supercontinuum generation," Opt. Express **21**, 18452–18460 (2013).
89. F. Poletti and P. Horak, "Description of ultrashort pulse propagation in multimode optical fibers," J. Opt. Soc. Am. B **25**, 1645–1654 (2008).
90. F. Poletti and P. Horak, "Dynamics of femtosecond supercontinuum generation in multimode fibers," Opt. Express **17**, 6134–6147 (2009).
91. R. Khakimov, I. Shavrin, S. Novotny, M. Kaivola, and H. Ludvigsen, "Numerical solver for supercontinuum generation in multimode optical fibers," Opt. Express **21**, 14388–14398 (2013).
92. A. Aalto, G. Genty, and J. Toivonen, "Extreme-value statistics in supercontinuum generation by cascaded stimulated Raman scattering," Opt. Express **18**, 1234–1239 (2010).
93. R. Buczyński, M. Klimczak, T. Stefaniuk, R. Kasztelanic, B. Siwicki, G. Stępniewski, J. Cimek, D. Pysz, and R. Stępień, "Optical fibers with gradient index nanostructured core," Opt. Express **23**, 25588–25596 (2015).
94. K. Krupa, A. Tonello, B. M. Shalaby, M. Fabert, A. Barthélémy, G. Millot, S. Wabnitz, and V. Couderc, "Spatial beam self-cleaning in multimode fibres," Nat. Photonics **11**, 237–241 (2017).
95. C. R. Petersen, P. M. Moselund, C. Petersen, U. Møller, and O. Bang, "Spectral-temporal composition matters when cascading supercontinua into the mid-infrared," Opt. Express **24**, 749–758 (2016).